Check for updates

In vivo reactive astrocyte imaging using [18F]SMBT-1 in tauopathy and familial Alzheimer's disease mouse models: A multi-tracer study

Yanyan Kong [a], Lei Cao [a,b], Jiao Wang [c], Junyi Zhuang [c], Fang Xie [a], Chuantao Zuo [a], Qi Huang [a], Kuangyu Shi [d], Axel Rominger [d], Ming Li [a], Ping Wu [a], Yihui Guan [a,*], Ruiqing Ni [b,d,e,*]

[a] PET Center, Huashan Hospital, Fudan University, Shanghai, China
[b] Inst. Regenerative Medicine, University of Zurich, Zurich, Switzerland
[c] Lab of Molecular Neural Biology, School of Life Sciences, Shanghai University, Shanghai, China
[d] Dept. Nuclear Medicine, Bern University Hospital, Bern, Switzerland
[e] Inst. Biomedical Engineering, ETH Zurich, Zurich, Switzerland

ARTICLE INFO

ABSTRACT

Background: Reactive astrocytes play an important role in the development of Alzheimer's disease and primary tauopathies. Here, we aimed to investigate the relationships between reactive astrocytes. Microgliosis and glucose metabolism with Tau and amyloid beta pathology by using multi-tracer imaging in widely used tauopathy and familial Alzheimer's disease mouse models.
Results: Positron emission tomography imaging using [18F]PM-PBB3 (tau), [18F]florbetapir (amyloid-beta), [18F]SMBT-1 (monoamine oxidase-B), [18F]DPA-714 (translocator protein) and [18F]fluorodeoxyglucose was carried out in 3- and 7-month-old rTg4510 tau mice, 5 × FAD familial Alzheimer's disease mice and wild-type mice. Immunofluorescence staining was performed to validate the pathological distribution in the mouse brain after in vivo imaging. We found increased regional levels of [18F]PM-PBB3, [18F]SMBT-1, and [18F]DPA-714 and hypoglucose metabolism in the brains of 7-month-old rTg4510 mice compared to age-matched wild-type mice. Increased [18F]SMBT-1 uptake was observed in the brains of 3, 7-month-old 5 × FAD mice, with elevated regional [18F]florbetapir and [18F]DPA-714 uptakes in the brains of 7-month-old 5 × FAD mice, compared to age-matched wild-type mice. Positive correlations were shown between [18F]SMBT-1 and [18F]PM-PBB3, [18F]DPA-714 and [18F]PM-PBB3 in rTg4510 mice, and between [18F]florbetapir and [18F]DPA-714 SUVRs in 5 × FAD mice.
Conclusion: In summary, these findings provide in vivo evidence that reactive astrocytes, microglial activation, and cerebral hypoglucose metabolism are associated with tau and amyloid pathology development in animal models of tauopathy and familial Alzheimer's disease.

1. Introduction

Neuroinflammation characterized by microglial activation and reactive astrocytes is an important pathological process in the progression of Alzheimer's disease (AD) and primary tauopathies [1]. Astrocytes play important roles in maintaining hemostasis, regulating blood flow, and supporting neuronal metabolism [1]. Astrocyte reactivity, as indicated by the plasma level of glial fibrillary acidic protein (GFAP), has been shown to be an early biomarker mediating the progression of AD and is correlated with the pathological hallmarks of AD, amyloid-β (Aβ)

and tau pathology [2–5]. Tau pathology epigenetically remodels neuron–glial cross-talk in AD [6]. Tufted astrocytes and astrocytic plaques are among the morphological hallmarks of primary tauopathies, including corticobasal degeneration and progressive supranuclear palsy [7]. Astrocytic 4R tau expression has been shown to drive astrocyte reactivity and dysfunction [7]. In addition, microglia and astrocytes are involved in the elimination of tau oligomer-containing synapses in AD [8]. In animal models of amyloidosis and tauopathy, chronic neuroinflammation has been shown to play an important role in neuroplasticity and cognitive function [9,10]. Tau accumulation in astrocytes

Table 1

Mouse models used in the study.

Model	Age (month)	[18F]SMBT-1	[18F]PM-PBB3	[18F]florbetapir	[18F]DPA-714	[18F]FDG
rTg4510	3	2F/4M	2F/4M		2F/4M	2F/5M
	7	2F/4M	2F/4M		2F/4M	2F/5M
5 × FAD	3	6 M		6 M	6 M	6 M
	7	6 M		6 M	6 M	6 M
Wild-type	3	6 M	6 M	8 M	6 M	8 M
	7	13 M	6 M	9 M	7 M	7 M

F, female; M, male;

of the dentate gyrus has been shown to induce neuronal dysfunction, memory deficits and cerebrovascular changes in animal models [11]. Transcriptomic associations of hippocampal GFAP-positive astrocytes have been reported in PS2APP mice with amyloidosis and in a P301S mouse model of tauopathy [4].

For imaging neuroinflammation, tracers targeting translocator protein (TSPO) are the most widely studied [12]. However, nonspecific binding and high cerebellar uptake of [11C]PK11195, [18F]DPA-714 and other TSPO tracers were noted. Tracers for other neuroinflammation targets, such as P2X7R [13], and colony-stimulating factor 1 receptor [14], are being developed [15]. Several positron emission tomography (PET) tracers for imaging reactive astrocytes have been developed. Among these targets, monoamine oxidase-B (MAO-B) has been a promising imaging target for reflecting reactive astrogliosis in AD and related dementias [16]. Several MAO-B tracers, including the irreversible inhibitor-based tracers [11C]deuterium-L-deprenyl (DED) and [18F]F-DED [17–19], reversible inhibitor-based tracers such as [18F]SMBT-1 [20] and [18F]GEH200449 [21], and the substrate-based MAO-B tracer [11C]Cou [22], have been developed. In addition, the mitochondrial imidazoline 2 binding site tracer [11C]BU99008 [3] and metabolism-targeting [11C]acetate [23] were used. Increased [18F]SMBT-1 brain uptake in Aβ-positive controls compared to Aβ-negative controls has been reported in patients with preclinical AD and is associated with Aβ load and plasma GFAP levels [20,24–26]. Thus far, a few MAO-B PET studies have been reported for reactive astrocytes in models of AD, including APP/PS1, PS2APP, and APPswe mice, using [11C]DED, [18F]F-DED [17–19] and [18F]SMBT-1 [27]. However, the in vivo reactive astrocyte PET pattern in the brains of tauopathy mice has not been determined.

Here, we aimed to evaluate reactive astrocytes in a widely used 4-repeat rTg4510 (P301L tau) mouse model [28] and in familial 5 × FAD mice with Aβ accumulation by using [18F]SMBT-1. We hypothesized that [18F]SMBT-1 is correlated with Aβ or tau accumulation in the brains of mouse models. In vivo PET using [18F]SMBT-1, [18F]PM-PBB3 (florzolotau, APN-1607) for tau [29], [18F]florbetapir for Aβ [30], [18F]DPA-714 for TSPO to represent microgliosis, and [18F]fluorodeoxyglucose (FDG) for cerebral glucose metabolism was carried out in rTg4510 tau mice [28], 5 × FAD mice [31], and age-matched wild-type mice at 3 months (prepathology) and 7 months (with Aβ or tau pathologies). Ex vivo immunofluorescence staining was performed on the mouse brain after the scan to validate the in vivo observations.

2. Methods and materials

2.1. Animal models

The animal models used in the study are summarized in Table 1. The rTg4510 mice (STOCK Tg(Camk2a-tTA)1Mmay Fgf14Tg(tetO-MAPT*P301L)4510Kha/J [28] and 5 × FAD mice (B6. Cg-Tg (APPSwFlLon, PSEN1*M146L*L286V)6799Vas/Mmjax) mice were used (JAX Laboratory) [32]. Wild-type C57BL6 mice were obtained from

Charles River, Germany, and Cavins Laboratory Animal Co., Ltd., of Changzhou. Mice were housed in ventilated cages inside a temperature-controlled room under a 12-h dark/light cycle. Pelleted food and water were provided ad libitum. Paper tissue and shelters were placed in cages for environmental enrichment. Animal model studies were performed following the American Research Institute (ARRIVE) guidelines 2.0. The PET imaging and experimental protocol were approved by the Institutional Animal Care and Ethics Committee of Fudan University and performed in accordance with the National Research Council's Guide for the Care and Use of Laboratory Animals.

2.2. Radiosynthesis

[18F]SMBT-1 (0.74 GBq/ml) was radiosynthesized via a fully automated procedure as previously described [20,27] using RD111 Eclipse Cyclotrons (Siemens, Germany). Briefly, [18F]SMBT-1 was radiosynthesized by 18F-nucleophilic substitution reaction using the precursor THK-5475 (MedChemExpress, China), followed by acid hydrolysis and alkali neutralization steps. [18F]PM-PBB3 (1.48 GBq/ml) was synthesized from an automatic synthesis module and a kit (APRINOIA therapeutics, China) [27,33]. [18F]florbetapir (0.56 GBq/ml) was radiosynthesized from its precursor via a fully automated procedure [34,35]. [18F]DPA-714 (1.48 GBq/ml) was labelled with fluorine-18 at its 2-fluoroethyl moiety after nucleophilic substitution of the corresponding linear analogue [36]. [18F]FDG (1.48 GBq/ml) was prepared in the radiochemistry facility under Good Manufacturing Practices requirements. The identities of the aforementioned final products were confirmed by comparison with the high-performance liquid chromatography retention times of the nonradioactive reference compounds obtained by coinjection using a Luna 5 μm C18(2) 100 Å (250 mm × 4.6 mm) column (Phenomenex). Acetonitrile and water (60:40) were used as solvents, and the flow rate was 1.0 ml/min. A radiochemical purity >95% was achieved for all the tracers (**SFig. 1** for [18F]PM-PBB3).

2.3. Small animal PET

PET experiments were performed using a Siemens Inveon PET/computed tomography (CT) system (Siemens Medical Solutions, United States) [37]. The mice underwent [18F]SMBT-1, [18F]florbetapir, [18F]PM-PBB3, [18F]DPA-714 and [18F]FDG scans sequentially, with 2 days of rest between the two scans. Mice were anaesthetized using 5% isoflurane and maintained using 1.5% isoflurane in medical oxygen (0.3–0.5 L/min) at room temperature with an isoflurane vaporizer (Molecular Imaging Products Company, USA) during the PET/CT procedure. The mice were positioned in a prone position on the heated imaging bed.

[18F]SMBT-1 small animal PET was performed as described earlier, and a single dose of tracers (~0.37 MBq/g body weight, 0.1–0.2 ml) was injected into the animals through the tail vein [27]. Static PET/CT images were obtained 10 min after intravenous administration of [18F]SMBT-1 at 60–70 min. PET/CT images were reconstructed using the ordered subsets expectation maximization 3D algorithm (OSEM3D), with a matrix size of 128 × 128 × 159 and a voxel size of 0.815 mm × 0.815 mm × 0.796 mm. Attenuation corrections derived from hybrid CT data were applied. To assess the specificity and selectivity of [18F]SMBT-1 in detecting MAO-B in the mouse brain, a blocking experiment was performed in 7-month-old wild-type male mice. Three mice were treated daily with the MAO-B inhibitor selegiline (intraperitoneal injection (i.p.) of selegiline, 10 mg/kg mouse weight) for 5 days before in vivo PET [18F]SMBT-1. Four age-matched WT mice (without selegiline treatment) were included in the control group for in vivo PET [18F]SMBT-1. On the 6th day, static PET/CT images were obtained of the mice in the selegiline-treated group and control group 10 min after intravenous administration of [18F]SMBT-1 at 60–70 min.

[18F]PM-PBB3, [18F]florbetapir, [18F]DPA-714, and [18F]FDG were used as described previously [27,35]. A single dose of tracers (~0.37
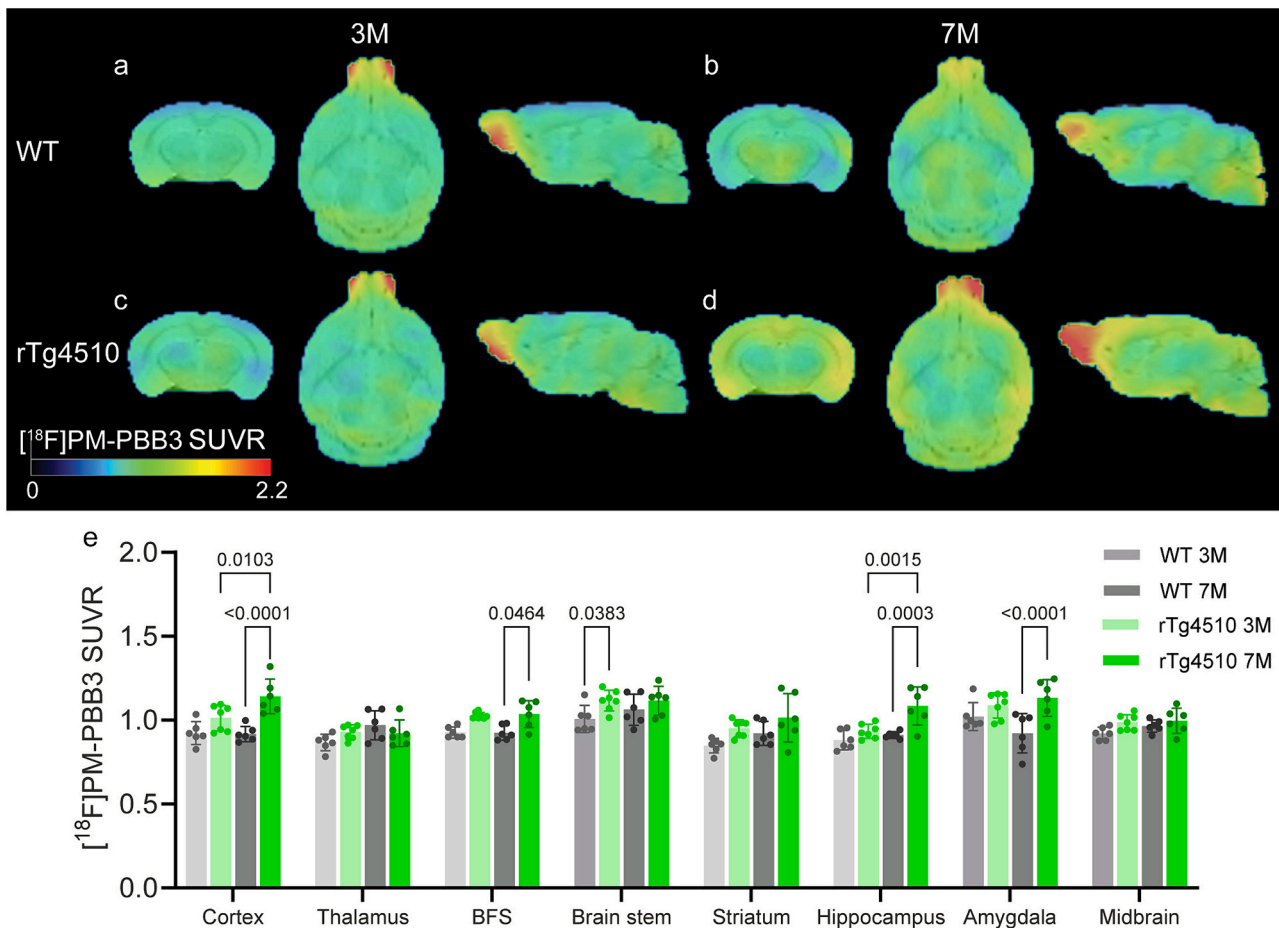
Fig. 1. **[^{18}F] PM-PBB3 brain uptake in 7-month-old rTg4510 mice compared to that in age-matched wild-type mice.** (**a-d**) [^{18}F]PM-PBB3 SUVR images of 3- and 7-month-old WT (a, b) and 3- and 7-month-old rTg4510 (c, d). The SUVR scale was 0–2.2. (**e**) Quantification of [^{18}F]PM-PBB3 using the cerebellum as a reference brain region.

MBq/g body weight, 0.1–0.2 ml) was injected into the animals through the tail vein. Static PET/CT images were obtained 10 min after intravenous administration of the tracer: [^{18}F]PM-PBB3 at 90–100 min, [^{18}F] florbetapir at 50–60 min, [^{18}F]DPA-714 at 40–50 min and [^{18}F]FDG at 60–70 min. PET/CT images were reconstructed, and attenuation corrections were applied as described above.

2.4. PET data analysis

PMOD 4.4 software was used for PET image analysis (PMOD Technologies Ltd., Switzerland). Radioactivity is presented as the standardized uptake value (SUV) (decay-corrected radioactivity per cm^3 divided by the injected dose per gram body weight). The volume of interest was defined based on a mouse MRI T$_2$-weighted image template as described earlier [27]. For [^{18}F]PM-PBB3, [^{18}F]florbetapir, [^{18}F]DPA-714, and [^{18}F]FDG, the cerebellum was chosen since it is the commonly used reference region for calculating the brain regional SUVR. However, few studies on [^{18}F]SMBT-1 in animal models have been reported. In our recent study, we performed dynamic [^{18}F]SMBT-1 imaging over 90 min in WT mice and amyloidosis mouse models and performed ex vivo staining for the MAO-B distribution in mouse brain slice. We found that the cerebellum is suitable as a reference brain region for computing the SUVR as the signal is relatively low in the cerebellum. Therefore, in this study, we used the cerebellum as a reference brain region for [^{18}F] SMBT-1 SUVR analysis [27]. A mask was applied for signals outside the mouse brain for illustration.

2.5. Immunofluorescence staining

Mice were anaesthetized with tribromoethanol, perfused with ice-cold 0.1 M phosphate-buffered saline (PBS, pH 7.4) and 4% paraformaldehyde in 0.1 M PBS (pH 7.4), fixed for 36 h in 4% paraformaldehyde (pH 7.4) and subsequently stored in 0.1 M PBS (pH 7.4) at 4 °C. For cryosectioning, the brain was placed in 30% sucrose in PBS (pH 7.4) until it sank. The brain was embedded in OCT gel (Tissue-Tek O.C.T., USA). Coronal brain sections (20 μm) were cut around the bregma 0 to −2 mm using a Leica CM1950 cryostat (Leica Biosystem, Germany). Detailed information on the reagents and antibodies used is provided in **STable 1**. For MAO-B immunofluorescence labelling, the sections were blocked in blocking buffer containing 3% bovine serum albumin, 0.4% Triton X-100, and 5% normal goat serum in PBS (pH 7.4) for 2 h at room temperature. After washing with PBS 3 × 10 min, the sections were incubated with primary antibodies against MAO-B (1:20; Sc-515,354; Santa Cruz Biotechnology) in blocking buffer overnight at 4 °C. For Aβ and phospho-Tau staining, the brains were fixed in paraffin according to a routine protocol. Coronal brain sections (3 μm) were cut using a Leica RM2016 Microtome (Leica Microsystems, Germany). The sections were first washed in PBS 3 × 10 min, followed by antigen retrieval for 20 min in citrate buffer (pH 6.0) at room temperature. After antigen retrieval in citrate buffer at room temperature, the sections were permeabilized and blocked in 3% bovine serum albumin for 30 min at room temperature with mild shaking. Paraffine-embedded sections were incubated overnight at 4 °C with primary antibodies against Aβ and phospho-Tau (Ser202, Thr205), as described earlier [38]. The next day,
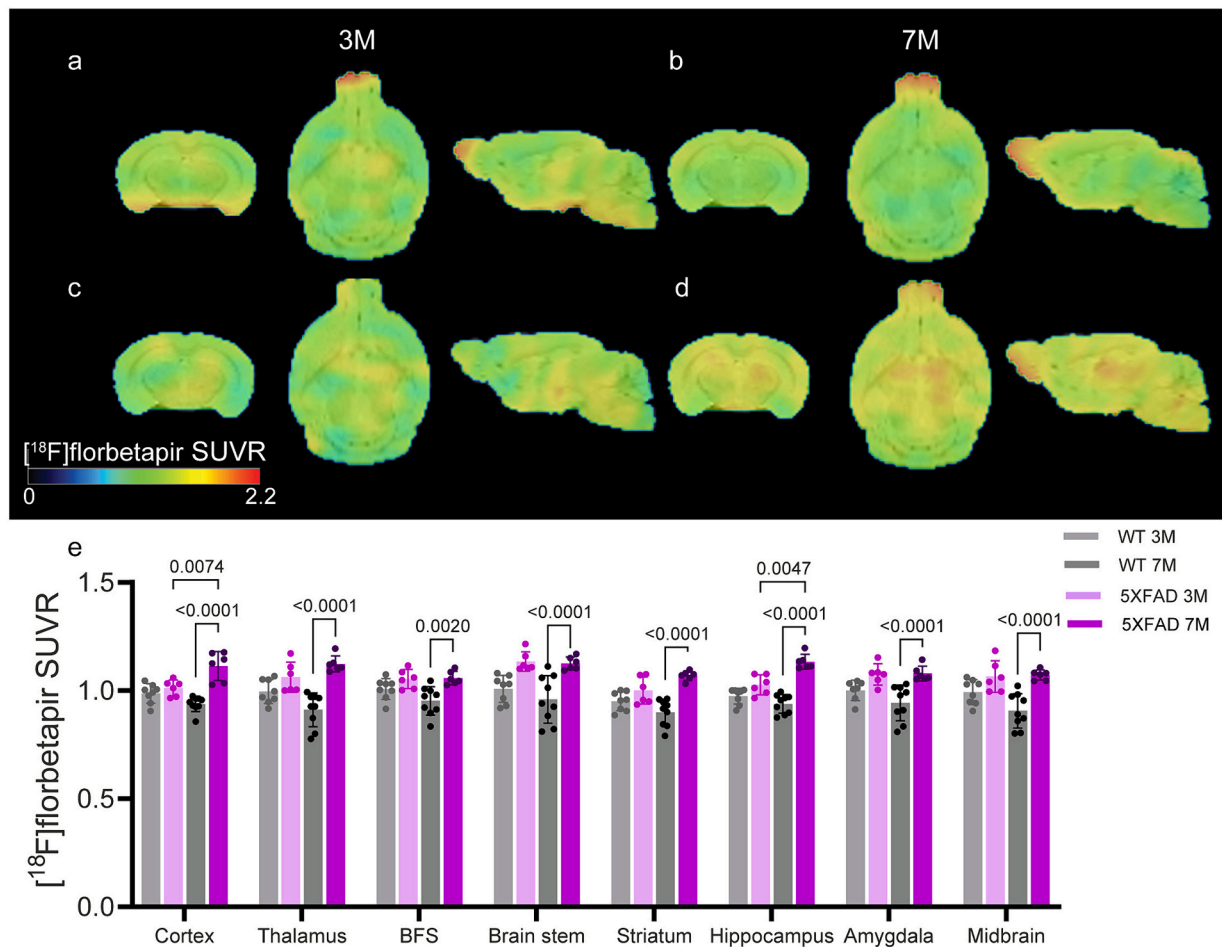
Fig. 2. [^{18}F] florbetapir brain uptake in 7-month-old 5 × FAD mice compared to that in age-matched wild-type mice. (**a-d**) [^{18}F]florbetapir SUVRs of 3- and 7-month-old WT (a, b) and 3- and 5 × FAD mice (c, d). The SUVR scale was 0–2.2. (**e**) Quantification of [^{18}F]florbetapir using the cerebellum as a reference brain region.

the slices were washed with PBS 3 × 5 min, incubated with secondary antibody for 2 h at room temperature and washed 3 × 5 min with PBS. The sections were incubated for 10 min in 4′,6-diamidino-2-phenyl-indole (DAPI) at room temperature and mounted with antifade mounting media [27]. The brain sections were imaged at ×20 magnification using a Pannoramic MIDI slide scanner (3DHISTECH) using the same acquisition settings for all brain slices. The immunofluorescence images were analysed by using ImageJ (NIH, U.S.A.). The signal intensity in the cortex and hippocampus of the brain slices was quantified (normalized to the values in wild-type mice).

2.6. Statistics

Two-way ANOVA with Dunnett's post hoc test was used for comparisons between multiple groups (GraphPad Prism 9.0, CA, USA). Two-way ANOVA with Sidak's post hoc test was used for comparisons between the blocking and baseline wild-type groups. A *p* value <0.05 was considered to indicate statistical significance. The data are shown as the mean ± standard deviation. Nonparametric Spearman's rank analysis was performed to assess the correlation between the SUVRs of different tracers.

3. Results

3.1. Regional tau accumulation in the brains of 7-month-old rTg4510 mice

We first characterized the tau distribution in the brains of rTg4510 mice at 3 and 7 months by PET using [^{18}F]PM-PBB3. rTg4510 mice are known to develop tau inclusions at approximately 4 months of age [28]. The cerebellum was validated in earlier studies as a reference region for the quantification of the SUVR [39,40]. Increased [^{18}F]PM-PBB3 SUVRs were detected in the cortex (*p* < 0.0001), basal forebrain system (BFS, *p* = 0.0464), brain stem (*p* = 0.0383), hippocampus (*p* = 0.0003), and amygdala (p < 0.0001) of 7-month-old rTg4510 mice (*n* = 6) compared with age-matched wild-type mice (n = 6) (Fig. 1). Increased [^{18}F]PM-PBB3 SUVRs were observed in the cortex (*p* = 0.0103) and hippocampus (*p* = 0.0015) of 7-month-old rTg4510 mice (n = 6) compared with 3-month-old rTg4510 mice (n = 6). No difference in the regional [^{18}F]PM-PBB3 SUVR was observed between 3-month-old rTg4510 mice (n = 6) and age-matched wild-type mice (n = 6).

3.2. Regional amyloid-beta deposition in the brains of 7-month-old 5 × FAD mice

Next, we assessed the distribution of amyloid pathology in 5 × FAD mice at 3 and 7 months of age. We used the cerebellum as a reference region for the quantification of the SUVR, as in earlier studies using [^{18}F] florbetapir imaging in this model [41]. The [^{18}F]florbetapir SUVRs were
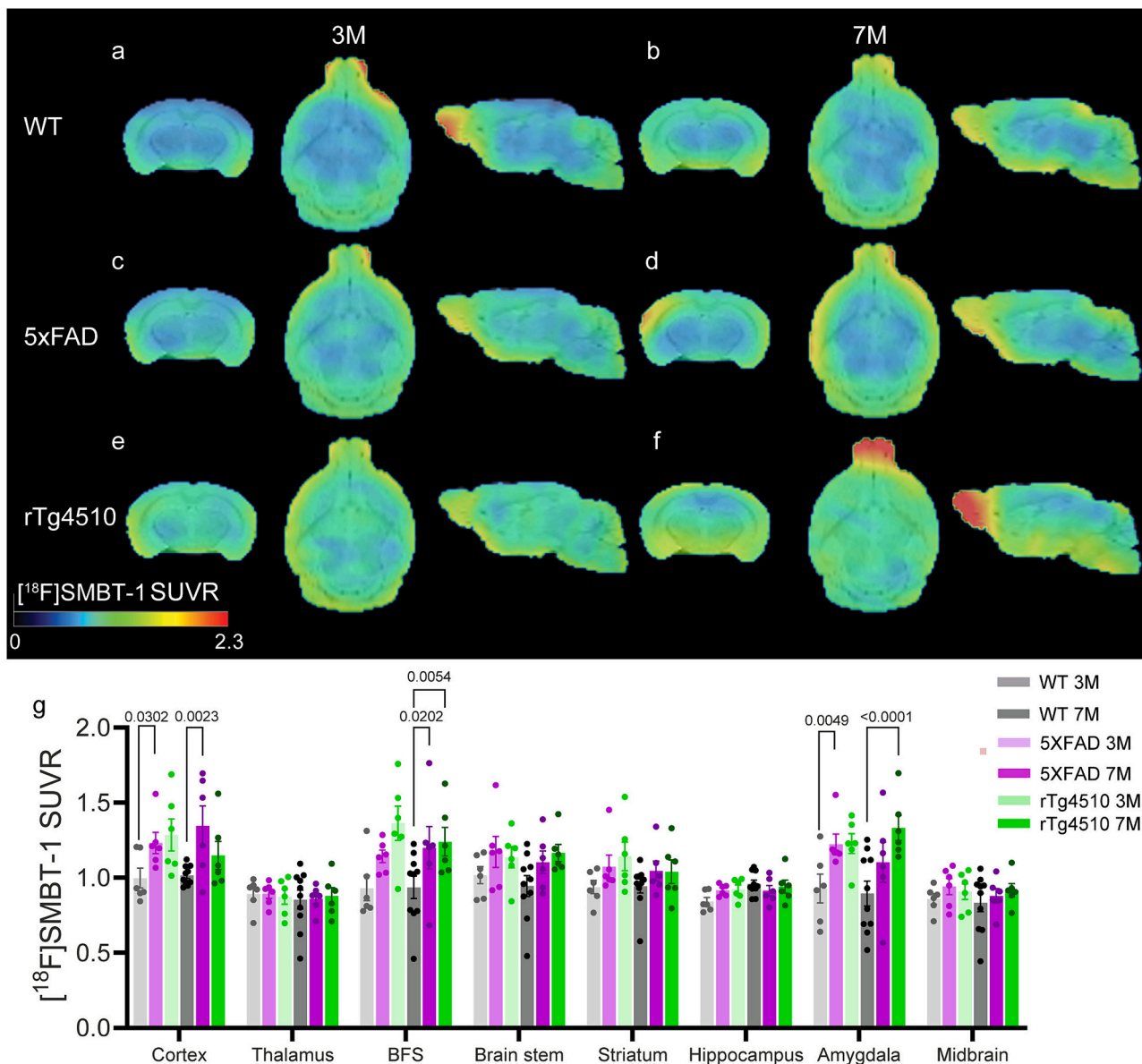
Fig. 3. Increased [^{18}F] SMBT-1 brain uptake in 7-month-old rTg4510 and 5 × FAD mice compared to age-matched wild-type mice. (a-f) SUVR images of 3- and 7-month-old WT (a, b), 3- and 7-month-old 5 × FAD (c, d), and rTg4510 mice (e, f). The SUVR scale was 0–2.3. (**g**) Quantification of [^{18}F]SMBT-1 uptake using the cerebellum as a reference region.

greater in all regions, including the cortex, thalamus, brainstem, striatum, hippocampus, amygdala, midbrain ($p < 0.0001$ for all 7 brain regions) and BFS ($p = 0.0020$), in 7-month-old 5 × FAD mice ($n = 6$) than in age-matched wild-type mice ($n = 9$). The [^{18}F]florbetapir SUVRs were greater in the cortex ($p = 0.0074$) and hippocampus ($p = 0.0047$) of 7-month-old 5 × FAD mice ($n = 6$) than in those of 3-month-old 5 × FAD mice ($n = 6$) (Fig. 2). No difference in the [^{18}F]florbetapir SUVR was observed between the brains of 3-month-old 5 × FAD mice ($n = 6$) and those of age-matched wild-type mice ($n = 8$).

3.3. Increased brain regional [^{18}F]SMBT-1 SUVRs in 5 × FAD and rTg4510 mice

[^{18}F]SMBT-1 is a relatively novel tracer for imaging MAO-B. Its specificity for MAO-B in the human brain has been demonstrated by an in vivo blocking study using selegiline [24]. To assess the in vivo specificity of [^{18}F]SMBT-1 in the mouse brain, we performed an in vivo blocking experiment using the MAO-B inhibitor selegiline, which has

been used in earlier blocking studies [24,42]. We chose the 5-day selegiline 10 mg/kg (i.p. injection) regimen based on earlier studies using a high dose of selegiline [43,44]. [^{18}F]SMBT-1 PET was performed on 7-month-old wild-type mice treated with selegiline and compared with those in the baseline group (7-month-old wild-type mice without treatment). Partial (25–30%) blocking was observed in the cortex, cerebellum and hippocampus of wild-type mice treated with selegiline ($n = 3$ blocking group) compared to wild-type mice without treatment ($n = 4$ baseline group, **SFig. 2**).

Next, we characterized the distribution of [^{18}F]SMBT-1 in 3- and 7-month-old rTg4510 mice, 5 × FAD mice and WT mice to assess the reactive astrocyte (MAO-B) pattern. The [^{18}F]SMBT-1 SUVR did not significantly differ between the 7 months-old wild-type mice ($n = 10$) and 3 months-old wild-type mice ($n = 6$). The [^{18}F]SMBT-1 SUVR was greater in the cortex ($p = 0.0023$) and BFS ($p = 0.0202$) of 7-month-old 5 × FAD mice ($n = 6$) than in age-matched wild-type mice ($n = 10$). The [^{18}F]SMBT-1 SUVR was greater in the BFS ($p = 0.0054$) and amygdala ($p < 0.0001$) of 7-month-old rTg4510 mice ($n = 6$) than in age-matched
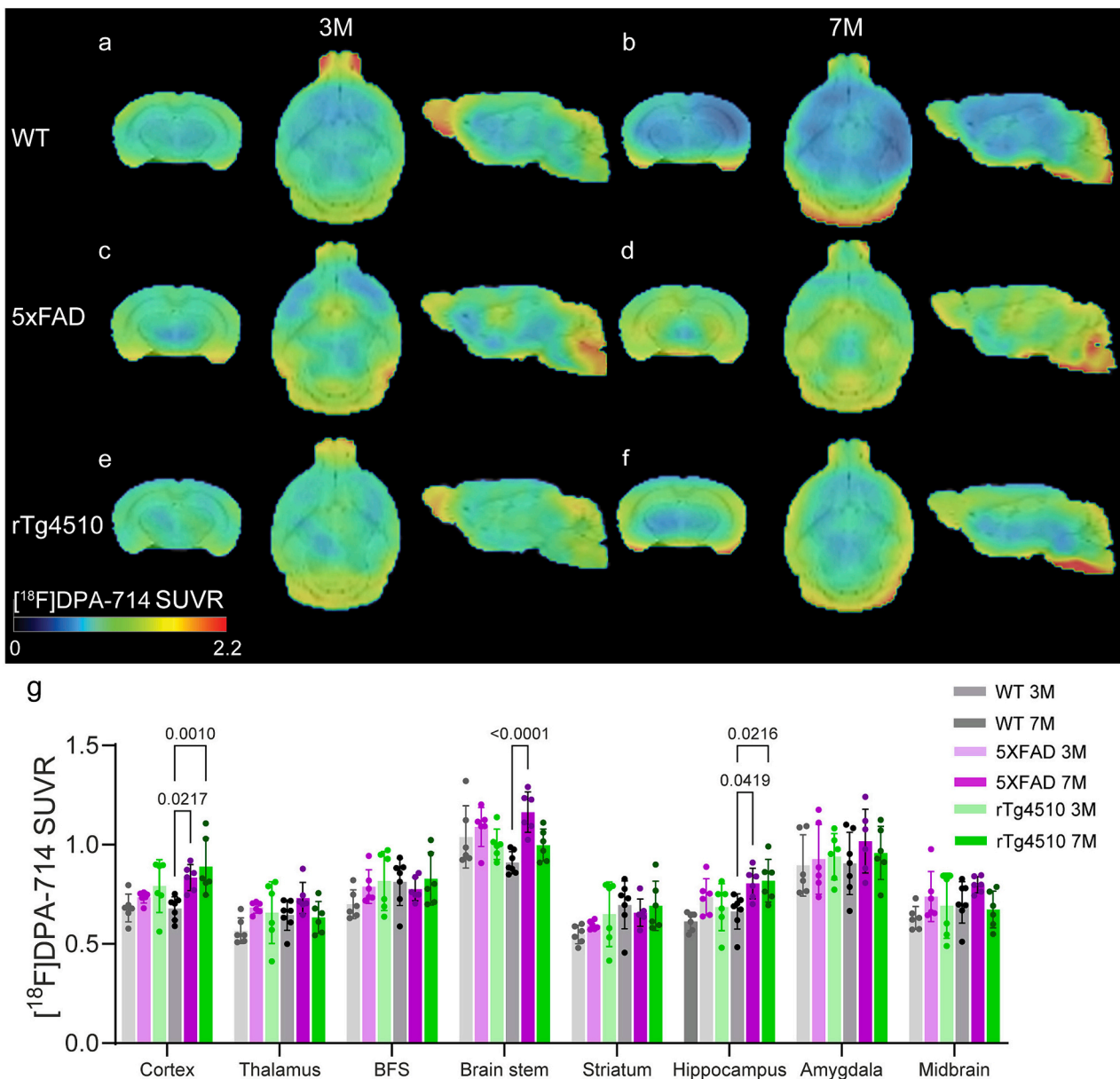
Fig. 4. Increased [¹⁸F] DPA-714 brain uptake in 7-month-old rTg4510 and 5 × FAD mice compared to age-matched wild-type mice. (**a-f**) SUVR images of 3- and 7-month-old WT (a, b), 3- and 7-month-old 5 × FAD mice (c, d), and rTg4510 mice (e, f). The SUVR scale was 0–2.2. (**g**) Quantification of [¹⁸F]DPA-714 using the cerebellum as a reference region.

wild-type mice (n = 10) (Fig. 3). The [¹⁸F]SMBT-1 SUVR was greater in the cortex ($p = 0.0302$) and amygdala ($p = 0.0049$) of 3-month-old 5 × FAD mice (n = 6) than in those of 3-month-old wild-type mice (n = 6) (Fig. 3). No significant difference in [¹⁸F]SMBT-1 SUVRs was detected in the brains of 3-month-old rTg4510 mice (n = 6) compared with those of 3-month-old wild-type mice (n = 6) (Fig. 3).

3.4. Increased brain regional [¹⁸F]DPA-714 SUVRs in 7-month-old 5 × FAD and rTg4510 mice

Next, we assessed the pattern of microglial activation by PET using [¹⁸F]DPA-714 in rTg4510 mice, 5 × FAD mice and WT mice at 3 and 7 months. Different reference brain regions, including the cerebellum [45–47], hypothalamus [48] and midbrain [49] (to avoid spillover), have been used for [¹⁸F]DPA-714 SUVR quantification in mouse models. Here, we used the cerebellum as a reference region because it was established for quantifying SUVRs in 5 × FAD and rTg4510 mice in

earlier studies [45,50], despite the known rather high signal in the cerebellum. We characterized the microglial distribution in rTg4510 mice, 5 × FAD mice and WT mice at 3 and 7 months by PET using [¹⁸F] DPA-714. The [¹⁸F]DPA-714 SUVR was greater in the cortex ($p = 0.0217$), brain stem ($p < 0.0001$) and hippocampus ($p = 0.0419$) of 7-month-old 5 × FAD mice ($n = 6$) than in age-matched wild-type mice ($n = 7$) (Fig. 4). A greater [¹⁸F]DPA-714 SUVR was detected in the cortex ($p = 0.0010$) and hippocampus ($p = 0.0216$) of 7-month-old rTg4510 mice (n = 6) than in age-matched wild-type mice (n = 7). No difference in [¹⁸F]DPA-714 SUVR was observed in the brains of 3-month-old 5 × FAD mice (n = 6) or rTg4510 mice (n = 6) compared to age-matched wild-type mice (n = 6). No difference in [¹⁸F]DPA-714 SUVR was detected in the brains of 7-month-old 5 × FAD mice compared with 3-month-old 5 × FAD mice (n = 6) or 7-month-old rTg4510 mice (n = 6) compared with 3-month-old rTg4510 mice (n = 6).
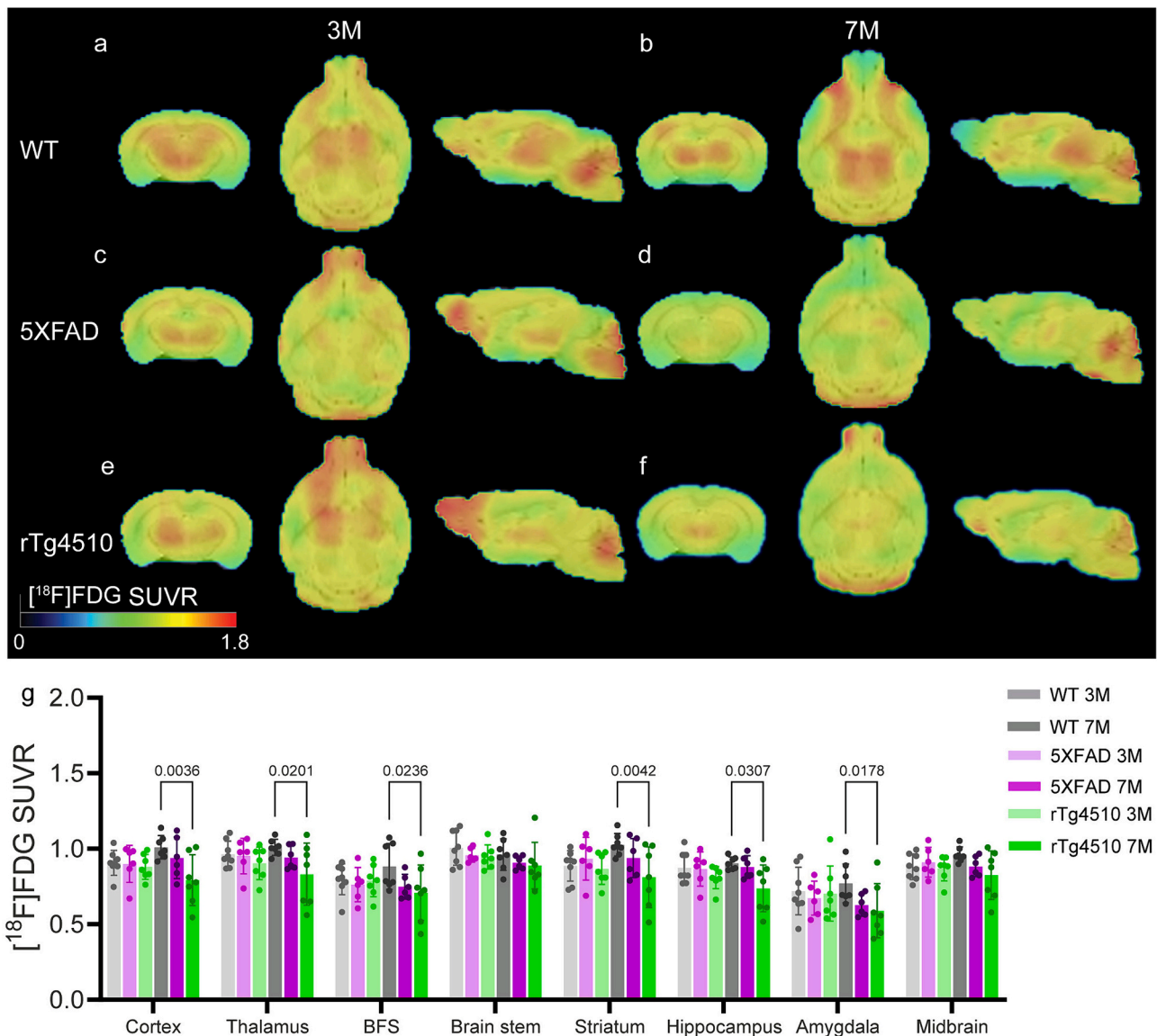
Fig. 5. [^{18}F] FDG brain uptake was lower in 7-month-old rTg4510 and 5 × FAD mice than in age-matched wild-type mice. (**a-f**) Images of SUVRs from 3- and 7-month-old WT (a, b), 3.7-month-old 5 × FAD mice (c, d), and rTg4510 mice (e, f). The SUVR scale was 0–1.8. (**g**) Quantification of [^{18}F]FDG using the cerebellum as a reference brain region.

3.5. Regional cerebral glucose hypometabolism in 7-month-old 5 × FAD and rTg4510 mice

To assess the changes in cerebral glucose hypometabolism and whether there are associations between these changes and other read-outs, we performed [^{18}F]FDG imaging in rTg4510 mice, 5 × FAD mice and WT mice at 3 and 7 months. The cerebellum was chosen as the reference region because it has been used in earlier studies [51]. Cerebral glucose metabolism ([^{18}F]FDG SUVR) in the cortex ($p = 0.0036$), thalamus ($p = 0.0201$), BFS ($p = 0.0236$), striatum ($p = 0.0042$), hippocampus ($p = 0.0307$) and amygdala ($p = 0.0178$) was detected in 7-month-old rTg4510 mice ($n = 7$) compared with age-matched wild-type mice ($n = 7$) (Fig. 5). The regional [^{18}F]FDG SUVR was lower in 7-month-old 5 × FAD mice ($n = 6$) than in age-matched wild-type mice ($n = 7$) but was not significantly different. No difference in [^{18}F]FDG SUVR was detected in the brains of 3-month-old 5 × FAD mice ($n = 6$) or rTg4510 mice ($n = 7$) compared with age-matched wild-type mice ($n = 8$).

Nonparametric Spearman's rank analysis was performed to assess the correlation between the SUVRs of different tracers. A negative correlation between regional [^{18}F]SMBT-1 and [^{18}F]FDG in 5 × FAD mice at 7 months and 3 months (12 mice, $p = 0.0001$, $r = -0.3805$, Fig. 6a). A positive correlation was detected between [^{18}F]SMBT-1 and [^{18}F]DPA-714 SUVR in 5 × FAD mice (12 mice, $p = 0.0274$, $r = 0.2252$, Fig. 6b), although the correlation coefficient r value is not high. The correlation r value was much stronger in the cortex between [^{18}F]SMBT-1 and [^{18}F]DPA-714 SUVRs of 5 × FAD mice at 7 months (6 mice, $p = 0.0333$, $r = 0.8857$, Fig. 6c). We found a positive correlation between regional [^{18}F]DPA-714 and [^{18}F]florbetapir SUVR in 5 × FAD mice (12 mice, $p < 0.0001$, $r = 0.4007$, Fig. 6d), while no correlation was observed between regional [^{18}F]SMBT-1 and [^{18}F]florbetapir in 5 × FAD mice (12 mice, $p = 0.5618$).

In rTg4510 tau model, we found a positive correlation between regional [^{18}F]SMBT-1 and [^{18}F]PM-PBB3 SUVR in rTg4510 mice (12 mice, $p < 0.0001$, $r = 0.4945$, Fig. 6e); and between regional [^{18}F]DPA-714 and [^{18}F]PM-PBB3 SUVR in rTg4510 mice (12 mice, $p < 0.0001$, $r = 0.4207$, Fig. 6f). A positive correlation was detected between regional [^{18}F] SMBT-1 and [^{18}F]DPA-714 SUVR in rTg4510 mice (12 mice, $p = 0.0172$, $r = 0.2427$, Fig. 6g), the correlation coefficient r value is rather low.
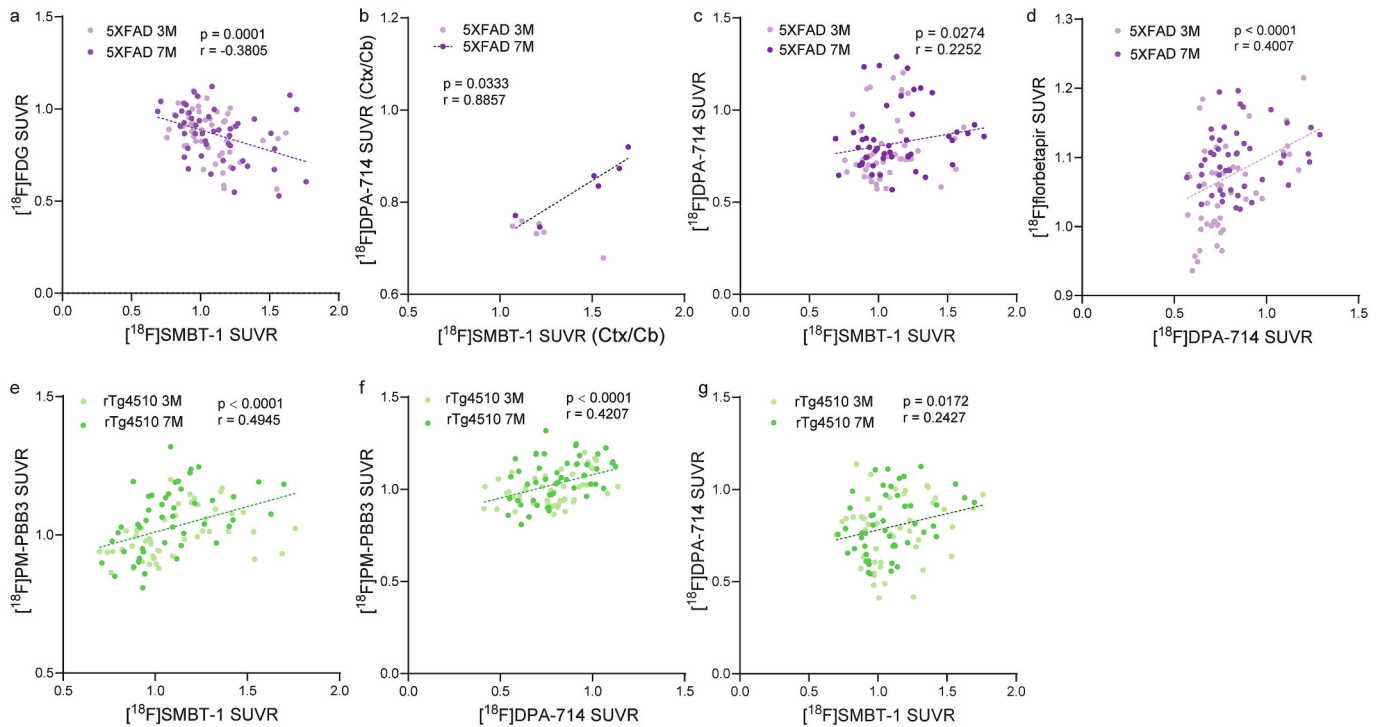
Fig. 6. Correlation between different imaging readouts in the brains of 5 × FAD and rTg4510 mice. (a) A negative correlation between [^{18}F]SMBT-1 and [^{18}F] FDG in the brain of 5 × FAD mice ($n = 12$, $p = 0.0001$, $r = 0.3805$); (b) A positive between [^{18}F]SMBT-1 and [^{18}F]DPA-714 SUVR in the cortex of 5 × FAD mice at 7 months ($n = 6$, $p = 0.0333$, $r = 0.8857$). (c) A positive correlation between [^{18}F]SMBT-1 and [^{18}F]DPA-714 SUVR in the brain of 5 × FAD mice ($n = 12$, $p = 0.0274$, $r = 0.2252$. (d) A positive correlation between [^{18}F]florbetapir and [^{18}F]DPA-714 SUVR in the brain of 5 × FAD mice (n = 12, $p < 0.0001$, $r = 0.4007$). (e) A positive correlation between [^{18}F]SMBT-1 and [^{18}F]PM-PBB3 SUVR in the brain of rTg4510 (n = 12, $p < 0.0001$, $r = 0.4945$). (f) A positive correlation between [^{18}F]DPA-714 and [^{18}F]PM-PBB3 SUVR in the brain of rTg4510 mice (n = 12, $p < 0.0001$, $r = 0.4207$). (g) A positive correlation between [^{18}F]SMBT-1 and [^{18}F]DPA-714 SUVR in the brain of rTg4510 mice (n = 12, $p = 0.0172$, $r = 0.2427$). Nonparametric Spearman's rank analysis was used for correlation analysis.

3.6. Immunofluorescence staining revealed pathologies in the mouse brain

Immunofluorescence staining was performed on the mice after they underwent in vivo imaging (Figs.7, 8). Phospho-Tau (p-Tau)-positive inclusions were detected in the cortex and hippocampus of 7-month-old rTg4510 mice, while no specific positive p-Tau signal was detected in the brains of age-matched WT mice. Immunofluorescence staining (Figs. 7e-i) revealed Aβ deposits in the cortex, hippocampus and thalamus of 7-month-old 5 × FAD mice, while no specific positive Aβ signals were detected in the brains of age-matched WT mice. The distribution of MAO-B in the brain slices of 7-month-old 5 × FAD mice appeared comparable to that in the brain slices of WT mice (SFig. 3). No significant increase in the level of MAO-B fluorescence intensity was detected in the cortex and hippocampus of the brain slices from 7-month-old rTg4510 mice compared with those from 7-month-old WT mice (Fig. 8).

4. Discussion

In the present study, we showed increased regional [^{18}F]SMBT-1 and [^{18}F]DPA-714 expression in the brains of 7-month-old rTg4510 mice and 5 × FAD mice, respectively, along with tau and Aβ pathology, compared to age-matched wild-type mice. The [^{18}F]SMBT-1 and [^{18}F] DPA-714 distributions appeared to be divergent both in the rTg4510 mice and in the 5 × FAD mice.

The use of PET has provided a quantitative in vivo imaging platform for tracking pathological amyloid and tau depositions and resultant pathophysiological changes in mouse models of AD and tauopathy. The [^{18}F]florbetapir pattern in 5 × FAD mice observed in our study is in line with the ex vivo staining of Aβ deposits and is consistent with the known Aβ plaque distribution pattern and earlier in vivo [^{18}F]florbetapir, [^{18}F] florbetaben, [^{18}F]FC119S, and [^{11}C] PIB imaging results in the brains of

5 × FAD mice [9,30,41,51–54]. The distribution pattern of [^{18}F]PM-PBB3 in rTg4510 mice corroborates the ex vivo staining results and the findings of previous studies in which [^{11}C]PBB3, [^{18}F]PM-PBB3 and [^{18}F]PI-2620 were used to detect increased uptake in tau-loaded brain regions [39,40,49,50,55,56]: Increased tau was found in cortical regions as well as in the hippocampus at 7 months and in association with the known pathological pattern of tau.

[^{18}F]SMBT-1 has shown high selectivity for MAO-B and low nonspecific binding in the brain, with >85% blocked by selegiline across the brain in humans in an earlier study [24]. Here, we found that the blocking effect in the mouse brain was only partial (<30%) when using selegiline, which is much less than that in humans. In addition, MAO-B might not be a specific marker for astrocyte reactivity due to its expression in astrocytes as well as in histaminergic and serotonergic neurons. In comparison, I2 binding sites (I$_2$BSs) exhibit specific expression in reactive astrocytes of the brain and may be a better biomarker for PET imaging of astrocyte reactivity. Sofar, an I$_2$BS tracer, [^{11}C]BU99008, has been evaluated in vivo [57]. Here, we found increased regional levels of [^{18}F]SMBT-1 in 7-month-old rTg4510 and in 3-, and 7-month-old 5 × FAD mice. No prior astrocytosis or MAO-B PET imaging studies have been reported in tauopathy mouse models or in the 5 × FAD mouse line. These findings are consistent with the findings of previous ex vivo staining and in vivo microscopy studies [58] revealing increased GFAP staining in the brains of 6-month-old rTg4510 mice [59]. Our finding of increased [^{18}F]SMBT-1 expression in 5 × FAD mice is consistent with the findings of a recent imaging study in which [^{11}C] acetate PET was used to image reactive astrocytes from 5 × FAD mice of similar age [23] and ex vivo characterization of elevated neuroinflammatory marker levels [9,60]. We found differences in the distribution pattern between the ex vivo MAO-B immunofluorescence staining pattern and in vivo [^{18}F]SMBT-1 signal in the brain: greater
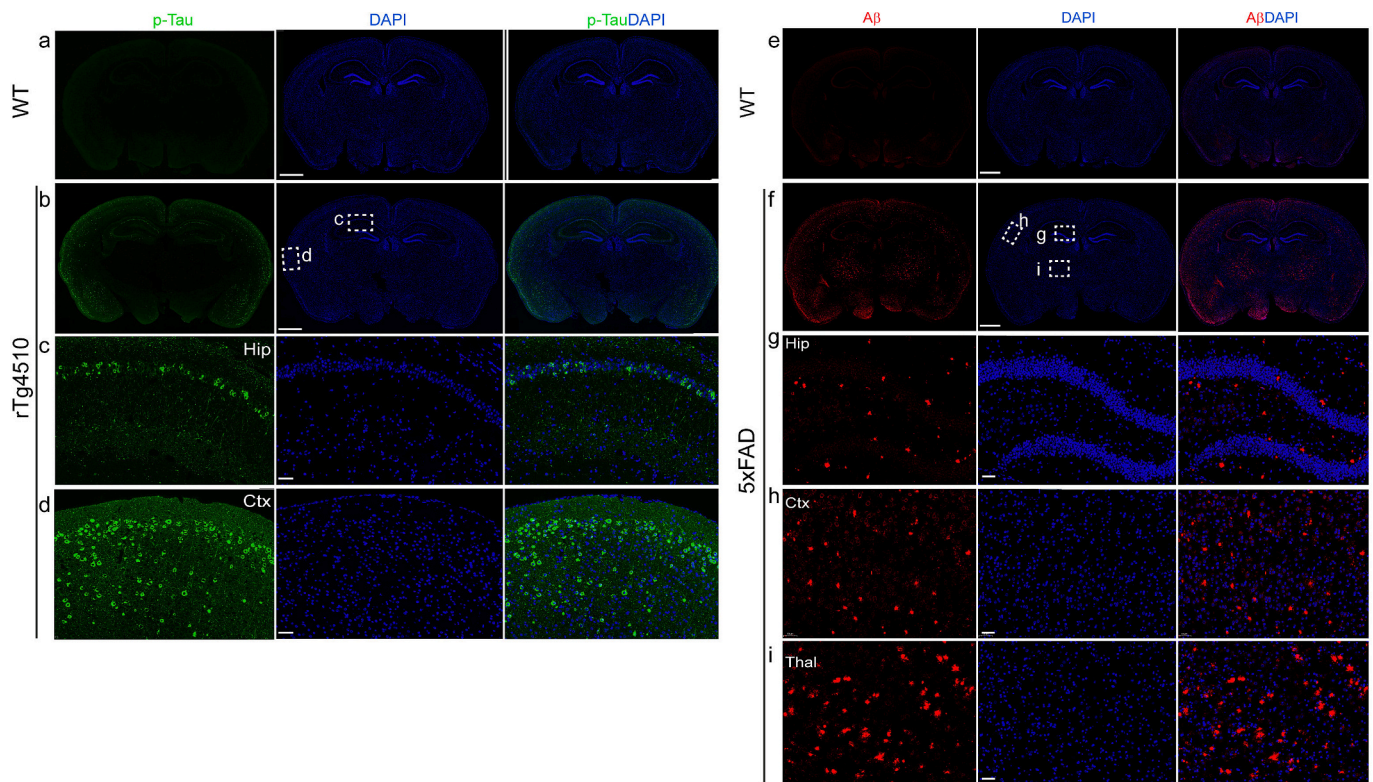
Fig. 7. Representative images of phospho-tau and amyloid-beta staining in the brains of 7-month-old WT, rTg4510, and 5 × FAD mice. (**a-d**) An overview and zoomed-in view of the phospho-Tau (p-Tau) staining of coronal brain slices from WT and rTg4510 mice revealed the presence of positive p-Tau inclusions (green) in the CA1 of hippocampus (Hip) and cortex (Ctx) of rTg4510 mice. (**e-i**) An overview and zoomed-in view of the amyloid-beta staining of coronal brain slices from WT and 5 × FAD mice. Amyloid-beta deposits (red) were observed in the dentate gyrus of hippocampus (Hip), cortex (Ctx), and thalamus (Thal) of 5 × FAD mice. Nuclei were counterstained with DAPI (blue). Scale bar = 1 mm (**a, b, e, f**) or 50 μm (**c, d, g-i**). (For interpretation of the references to colour in this figure legend, the reader is referred to the web version of this article.)

immunofluorescence was found in the hippocampus than in the cortical region of the mouse brain slices, opposite to the in vivo pattern. In addition, no significant difference was found between ex vivo MAO-B immunofluorescence between different mouse groups. One probable reason is that MAO-B is an enzyme, and the activity measured in vivo might be different from the level measured ex vivo. In earlier studies, both association of in vivo MAO-B signal (such as [18F]F-DED) with ex vivo MAO-B expression in GFAP-positive astrocytes [18], and lack of in vivo – ex vivo association [17,19] has been reported in animal models. Possible reasons for the different observation include the choice of antibody for staining, different quantification, as well as both cellular sources of MAO-B (astroglial and neuronal).

The time course of microglial changes has been well characterized by in vivo TSPO imaging in different mouse models. Including PS2APP mice, APP/PS1 mice, and the TgF344 rat model [18,61,62] and ex vivo by using staining [63,64] and transcriptomics. Our observation of increased [18F]DPA-714 in 7-month-old 5 × FAD and rTg4510 mice is in line with previous reports. Increased cerebral uptake has been shown using [18F]DPA-714 [65] at 8 months and [11C]PBR28 [66] at 6 months in 5 × FAD mice. Moreover, TSPO colocalizes with iba1-positive reactive microglia but not GFAP-positive astrocytes in the brains of 6-month-old 5 × FAD mice [66]. Increased levels of [18F]DPA-714 [49], [11C]AC-5216 [50], and [18F]FEBMP [67] have been reported in rTg4510 mice at 7 months of age. However, the exact mechanism by which TSPO signalling occurs is still unclear: TSPO is known to be expressed on both microglia and astrocytes. A previous study showed that astrocytic TSPO upregulation occurs before microglial TSPO upregulation in TgF344 rats [68]. Another study suggested that TSPO upregulation is selective for proinflammatory polarized astrocytes and microglia through the use of profiling and immunostaining [69]. Notably, an earlier study indicated

sex differences in microglial activation by TSPO imaging in Aβ but not in tau animal models [70].

We showed that, compared with those in age-matched controls, there was reduced [18F]FDG uptake in the brains of rTg4510 mice but not in those of 7-month-old 5 × FAD mice. These findings are in line with the observed hypometabolism in the brains of 7-month-old rTg4510 mice [49,71]. Perfusion, functional resting-state brain network and metabolic connectivity changes have been reported in rTg4510 mice [58,72,73]. Inconsistent FDG results have been reported in 5 × FAD mice. A recent characterization study revealed no overt metabolic changes caused by [18F]FDG uptake in 5 × FAD mice at 4, 6 or 12 months of age [74]. Another study showed some edgewise differences, but no regions showed differences in 5 × FAD mice at 6 months of age for either sex [75]. In addition, an increased cerebral level of [18F]FDG was reported in 5 × FAD mice at 11 months of age [30]. In contrast, two other studies reported decreased [18F]FDG in 5 × FAD mice at 7 and 12 months of age [76] and at 13 months [77] (no difference was observed in 5 × FAD mice). One possible reason for this complexity is that the increased activity and metabolic changes in microglia in amyloidosis or tau mouse brains are associated with overall [18F]FDG glucose uptake [78,79]. The inconsistency in the [18F]FDG PET results in the rodent brain might stem from the variability in temperature, anaesthesia depth, physiological condition of the mice, sex of the mice, etc. It has also been suggested that the use of the cerebellum as a reference region may result in enhanced hypermetabolism in AD mouse models, as the cerebellum might also be subject to metabolic changes [51].

Previous study revealed a positive correlation between in vivo uptake of [18F]SMBT-1 with amyloid and tau tracer uptakes in AD patients and control cases, indicating an association between MAO-B alteration with AD pathologies [25]. Here we found a positive correlation between
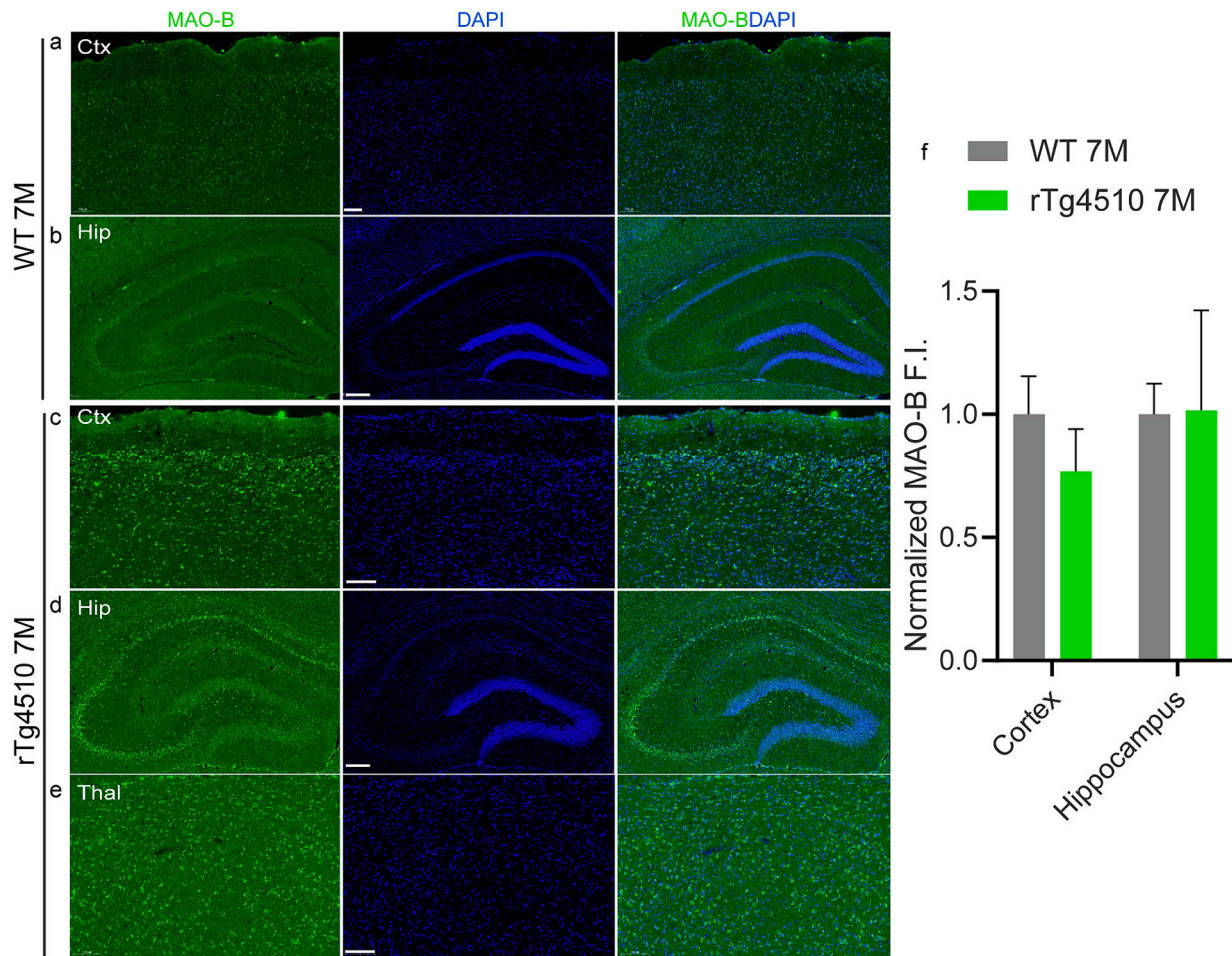
Fig. 8. Representative MAO-B staining of brain tissue from 7-month-old WT, rTg4510, and 5 × FAD mice. (a-d) A zoomed-in view and quantification revealing the distribution and levels of MAO-B (green) in the hippocampus (Hip), cortex (Ctx) and thalamus (Thal) of WT (a, b), rTg4510 (c-e). Nuclei were counterstained with DAPI (blue). Scale bar = 100 μm (**a, c, e) or** 200 μm (**b, d**). (For interpretation of the references to colour in this figure legend, the reader is referred to the web version of this article.)

regional SUVR of [18F]SMBT-1 and [18F]PM-PBB3 in rTg4510 mice ($p < 0.0001, r = 0.4945$). It is noted that there is no correlation between [18F]SMBT-1 and [18F]PM-PBB3 within a single region. Our data did not indicate a correlation between regional SUVR of [18F]SMBT-1 and [18F]florbetapir in 5 × FAD mice. Similarly, we also did not observe correlation between regional SUVR of [18F]SMBT-1 and [18F]florbetapir in our recent study using another amyloidosis mouse model (APP/PS1 mice) [27].

The regional TSPO tracer [18F]DPA-714 SUVR appeared to positively correlate with [18F]florbetapir SUVR in 5 × FAD mice ($p < 0.0001, r = 0.4007$) as well as with [18F]PM-PBB3 in rTg4510 mice ($p < 0.0001, r = 0.4207$). Similar positive correlations between TSPO tracer uptake with amyloid and tau tracer uptake have been reported in earlier studies in earlier studies in both amyloidosis as well as tau transgenic mice [27,49,80,81]. Moreover, we found a positive correlation between regional [18F]SMBT-1 and [18F]DPA-714 SUVRs in both 5 × FAD mice and in rTg4510 mice, with is more robust in the cortex of 5 × FAD mice at 7 months with higher amyloid deposition ($p = 0.0333, r = 0.8857$).

The limitations of the current study include the lack of a longitudinal (instead of cross-sectional) study design. In addition, the scans performed in this study were static, and dynamic scans could provide more accurate quantification at the expense of a much longer scanning time. Moreover, as a multitracer study design, animals were subjected to anaesthesia 4 or 5 times for all imaging exams. Although the mice were allowed to rest for 2 days between scans, anaesthesia might have affected tracer uptake [82]. Moreover, a recent study showed that

anaesthesia using sevoflurane reduced the in vivo binding of [11C]L-deprenyl-D2 to MAO-B in nonhuman primates [83]. It is possible that isoflurane could also affect the tracer retention of [18F]SMBT-1 in mice during PET scans. Further study is needed to elucidate the influence of different anaesthetics on MAO-B PET tracer uptake in rodents.

In conclusion, the present study provided in vivo imaging evidence for regional reactive astrocytes in the brains of 5 × FAD and rTg4510 mice, as did Aβ and tau deposition, hypoglucose metabolism and activated microglia. [18F]SMBT-1 imaging in these two models might be useful for in vivo evaluation of treatments targeting astrocytes for tauopathy and AD.

Ethics approval and consent to participate

This study in animal models was carried out in compliance with the ARRIVE guidelines 2.0. All the experimental protocols were approved by the Institutional Animal Care and Ethics Committee of Fudan University. All methods were carried out in accordance with the National Research Council's Guide for the Care and Use of Laboratory Animals.

Consent to participate

Not applicable.

Consent for publication

Not Applicable.

Authors' contributions

The study was designed by YK and RN. KY and QH performed the radiolabelling, HPLC, and small animal PET experiments. CZ provided the protocol. LC and RN analysed the small animal PET data. FX, JX, ML, and YY prepared the tracers. YK, LC, and RN wrote the first draft. KY, LC, and RN contributed to the data interpretation. YK, YG, and RN provided funding and access to infrastructure. All the authors contributed to the revision of the manuscript and approved the final manuscript.

CRediT authorship contribution statement

Yanyan Kong: Writing – review & editing, Writing – original draft, Investigation, Funding acquisition, Data curation, Conceptualization. **Lei Cao:** Writing – review & editing, Writing – original draft, Visualization, Formal analysis. **Jiao Wang:** Writing – review & editing, Investigation, Data curation. **Junyi Zhuang:** Writing – review & editing, Investigation, Data curation. **Fang Xie:** Writing – review & editing. **Chuantao Zuo:** Writing – review & editing, Resources, Methodology. **Qi Huang:** Writing – review & editing, Methodology, Investigation. **Kuangyu Shi:** Writing – review & editing. **Axel Rominger:** Writing – review & editing. **Ming Li:** Writing – review & editing. **Ping Wu:** Writing – review & editing, Methodology, Investigation. **Yihui Guan:** Writing – review & editing, Resources. **Ruiqing Ni:** Writing – review & editing, Writing – original draft, Supervision, Project administration, Funding acquisition, Formal analysis, Conceptualization.

Declaration of competing interest

The authors declare that they have no competing interests.

Data availability

The datasets used and/or analysed during the current study are available from the corresponding author upon reasonable request.

Appendix A. Supplementary data

Supplementary data to this article can be found online at https://doi.org/10.1016/j.jns.2024.123079.

References

[1] R. Patani, G.E. Hardingham, S.A. Liddelow, Functional roles of reactive astrocytes in neuroinflammation and neurodegeneration, Nat. Rev. Neurol. 19 (7) (2023) 395–409.

[2] W. Pelkmans, M. Shekari, A. Brugulat-Serrat, G. Sánchez-Benavides, C. Minguillón, K. Fauria, J.L. Molinuevo, O. Grau-Rivera, A. González Escalante, G. Kollmorgen, M. Carboni, N.J. Ashton, H. Zetterberg, K. Blennow, M. Suarez-Calvet, J.D. Gispert, Astrocyte biomarkers GFAP and YKL-40 mediate early Alzheimer's disease progression, Alzheimers Dement 20 (1) (2023) 483–493.

[3] J.P. Ferrari-Souza, P.C.L. Ferreira, B. Bellaver, C. Tissot, Y.T. Wang, D.T. Leffa, W. S. Brum, A.L. Benedet, N.J. Ashton, M.A. De Bastiani, A. Rocha, J. Therriault, F. Z. Lussier, M. Chamoun, S. Servaes, G. Bezgin, M.S. Kang, J. Stevenson, N. Rahmouni, V. Pallen, N.M. Poltronetti, W.E. Klunk, D.L. Tudorascu, A.D. Cohen, V.L. Villemagne, S. Gauthier, K. Blennow, H. Zetterberg, D.O. Souza, T.K. Karikari, E.R. Zimmer, P. Rosa-Neto, T.A. Pascoal, Astrocyte biomarker signatures of amyloid-β and tau pathologies in Alzheimer's disease, Mol. Psychiatry 27 (11) (2022) 4781–4789.

[4] M.A. De Bastiani, B. Bellaver, W.S. Brum, D.G. Souza, P.C.L. Ferreira, A.S. Rocha, G. Povala, J.P. Ferrari-Souza, A.L. Benedet, N.J. Ashton, T.K. Karikari, H. Zetterberg, K. Blennow, P. Rosa-Neto, T.A. Pascoal, E.R. Zimmer, Hippocampal GFAP-positive astrocyte responses to amyloid and tau pathologies, Brain Behav. Immun. 110 (2023) 175–184.

[5] Z. Tang, Z. Chen, M. Guo, Y. Peng, Y. Xiao, Z. Guan, R. Ni, X. Qi, NRF2 deficiency promotes ferroptosis of astrocytes mediated by oxidative stress in Alzheimer's disease, Mol. Neurobiol. (2024).

[6] L.T. Zhou, D. Liu, H.C. Kang, L. Lu, H.Z. Huang, W.Q. Ai, Y. Zhou, M.F. Deng, H. Li, Z.Q. Liu, W.F. Zhang, Y.Z. Hu, Z.T. Han, H.H. Zhang, J.J. Jia, A.K. Sarkar, S. Sharaydeh, J. Wang, H.Y. Man, M. Schilling, L. Bertram, Y. Lu, Z. Guo, L.Q. Zhu, Tau pathology epigenetically remodels the neuron-glial cross-talk in Alzheimer's disease, Sci. Adv. 9 (16) (2023) eabq7105.

[7] L.A. Ezerskiy, K.M. Schoch, C. Sato, M. Beltcheva, K. Horie, F. Rigo, R. Martynowicz, C.M. Karch, R.J. Bateman, T.M. Miller, Astrocytic 4R tau expression drives astrocyte reactivity and dysfunction, JCI Insight 7 (1) (2022) e152012.

[8] R.N. Taddei, R. Perbet, A. Mate de Gerando, A.E. Wiedmer, M. Sanchez-Mico, T. Connors Stewart, A. Gaona, A. Melloni, A.C. Amaral, K. Duff, M.P. Frosch, T. Gómez-Isla, Tau oligomer-containing synapse elimination by microglia and astrocytes in Alzheimer disease, JAMA Neurol. 80 (11) (2023) 1209–1221.

[9] D. Lecca, Y.J. Jung, M.T. Scerba, I. Hwang, Y.K. Kim, S. Kim, S. Modrow, D. Tweedie, S.C. Hsueh, D. Liu, W. Luo, E. Glotfelty, Y. Li, J.Y. Wang, Y. Luo, B. J. Hoffer, D.S. Kim, R.A. McDevitt, N.H. Greig, Role of chronic neuroinflammation in neuroplasticity and cognitive function: a hypothesis, Alzheimers Dement. 18 (11) (2022) 2327–2340.

[10] B. Dejanovic, T. Wu, M.C. Tsai, D. Graykowski, V.D. Gandham, C.M. Rose, C. E. Bakalarski, H. Ngu, Y. Wang, S. Pandey, M.G. Rezzonico, B.A. Friedman, R. Edmonds, A. De Mazière, R. Rakosi-Schmidt, T. Singh, J. Klumperman, O. Foreman, M.C. Chang, L. Xie, M. Sheng, J.E. Hanson, Complement C1q-dependent excitatory and inhibitory synapse elimination by astrocytes and microglia in Alzheimer's disease mouse models, Nat Aging 2 (9) (2022) 837–850.

[11] K. Richetin, P. Steullet, M. Pachoud, R. Perbet, E. Parietti, M. Maheswaran, S. Eddarkaoui, S. Bégard, C. Pythoud, M. Rey, R. Caillierez, Q.D. K, S. Halliez, P. Bezzi, L. Buée, G. Leuba, M. Colin, N. Toni, N. Déglon, Tau accumulation in astrocytes of the dentate gyrus induces neuronal dysfunction and memory deficits in Alzheimer's disease, Nat. Neurosci. 23 (12) (2020) 1567–1579.

[12] W.C. Kreisl, M.J. Kim, J.M. Coughlin, I.D. Henter, D.R. Owen, R.B. Innis, PET imaging of neuroinflammation in neurological disorders, Lancet Neurol. 19 (11) (2020) 940–950.

[13] P.R. Territo, J.A. Meyer, J.S. Peters, A.A. Riley, B.P. McCarthy, M. Gao, M. Wang, M.A. Green, Q.H. Zheng, G.D. Hutchins, Characterization of (11)C-GSK1482160 for targeting the P2X7 receptor as a biomarker for neuroinflammation, J. Nucl. Med. 58 (3) (2017) 458–465.

[14] A.G. Horti, R. Naik, C.A. Foss, I. Minn, V. Misheneva, Y. Du, Y. Wang, W. B. Mathews, Y. Wu, A. Hall, C. LaCourse, H.H. Ahn, H. Nam, W.G. Lesniak, H. Valentine, O. Pletnikova, J.C. Troncoso, M.D. Smith, P.A. Calabresi, A. V. Savonenko, R.F. Dannals, M.V. Pletnikov, M.G. Pomper, PET imaging of microglia by targeting macrophage colony-stimulating factor 1 receptor (CSF1R), Proc. Natl. Acad. Sci. U. S. A. 116 (5) (2019) 1686–1691.

[15] R. Zhou, B. Ji, Y. Kong, L. Qin, W. Ren, Y. Guan, R. Ni, PET imaging of Neuroinflammation in Alzheimer's disease, Front. Immunol. 12 (2021) 3750.

[16] M. Jaisa-Aad, C. Muñoz-Castro, M.A. Healey, B.T. Hyman, A. Serrano-Pozo, Characterization of monoamine oxidase-B (MAO-B) as a biomarker of reactive astrogliosis in Alzheimer's disease and related dementias, Acta Neuropathol. 147 (1) (2024) 66.

[17] E. Rodriguez-Vieitez, R. Ni, B. Gulyás, M. Tóth, J. Häggkvist, C. Halldin, L. Voytenko, A. Marutle, A. Nordberg, Astrocytosis precedes amyloid plaque deposition in Alzheimer APPswe transgenic mouse brain: a correlative positron emission tomography and in vitro imaging study, Eur. J. Nucl. Med. Mol. Imaging 42 (7) (2015) 1119–1132.

[18] A. Ballweg, C. Klaus, L. Vogler, S. Katzdobler, K. Wind, A. Zatcepin, S.I. Ziegler, B. Secgin, F. Eckenweber, B. Bohr, A. Bernhardt, U. Fietzek, B.S. Rauchmann, S. Stoecklein, S. Quach, L. Beyer, M. Scheifele, M. Simmet, E. Joseph, S. Lindner, I. Berg, N. Koglin, A. Mueller, A.W. Stephens, P. Bartenstein, J.C. Tonn, N.L. Albert, T. Kümpfel, M. Kerschensteiner, R. Perneczky, J. Levin, L. Paeger, J. Herms, M. Brendel, [^{18}F]F-DED PET imaging of reactive astrogliosis in

neurodegenerative diseases: preclinical proof of concept and first-in-human data, J. Neuroinflammation 20 (1) (2023) 68.

[19] M. Olsen, X. Aguilar, D. Sehlin, X.T. Fang, G. Antoni, A. Erlandsson, S. Syvänen, Astroglial responses to amyloid-Beta progression in a mouse model of Alzheimer's disease, Mol. Imaging Biol. 20 (4) (2018) 605–614.

[20] R. Harada, Y. Hayakawa, M. Ezura, P. Lerdsirisuk, Y. Du, Y. Ishikawa, R. Iwata, M. Shidahara, A. Ishiki, A. Kikuchi, H. Arai, Y. Kudo, K. Yanai, S. Furumoto, N. Okamura, (18)F-SMBT-1: a selective and reversible PET tracer for monoamine oxidase-B imaging, J. Nucl. Med. 62 (2) (2021) 253–258.

[21] S. Nag, Z. Jia, M. Svedberg, A. Jackson, R. Ahmad, S. Luthra, K. Varnäs, L. Farde, C. Halldin, Synthesis and autoradiography of novel F-18 labeled reversible radioligands for detection of monoamine oxidase B, ACS Chem. Neurosci. 11 (24) (2020) 4398–4404.

[22] L.R. Drake, A.F. Brooks, A.J. Mufarreh, J.M. Pham, R.A. Koeppe, X. Shao, P.J. H. Scott, M.R. Kilbourn, Deuterium kinetic isotope effect studies of a potential in vivo metabolic trapping agent for monoamine oxidase B, ACS Chem. Neurosci. 9 (12) (2018) 3024–3027.

[23] M.-H. Nam, H.Y. Ko, D. Kim, S. Lee, Y.M. Park, S.J. Hyeon, W. Won, J.-I. Chung, S. Y. Kim, H.H. Jo, K.T. Oh, Y.-E. Han, G.-H. Lee, Y.H. Lee, H. Kim, J. Heo, M. Bhalla, K.J. Kim, J. Kwon, T.D. Stein, M. Kong, H. Lee, S.E. Lee, S.-J. Oh, J.-H. Chun, M.-A. Park, K.D. Park, H. Ryu, M. Yun, C.J. Lee, Visualizing reactive astrocyte-neuron interaction in Alzheimer's disease using 11C-acetate and 18F-FDG, Brain (2023) awad037.

[24] V.L. Villemagne, R. Harada, V. Doré, S. Furumoto, R. Mulligan, Y. Kudo, S. Burnham, N. Krishnadas, S. Bozinovski, K. Huang, B.J. Lopresti, K. Yanai, C. C. Rowe, N. Okamura, First-in-humans evaluation of (18)F-SMBT-1, a novel (18)F-labeled monoamine oxidase-B PET tracer for imaging reactive Astrogliosis, J. Nucl. Med. 63 (10) (2022) 1551–1559.

[25] V.L. Villemagne, R. Harada, V. Dore, S. Furumoto, R. Mulligan, Y. Kudo, S. Burnham, N. Krishnadas, P. Bourgeat, Y. Xia, S. Laws, S. Bozinovski, K. Huang, M.D. Ikonomovic, J. Fripp, K. Yanai, N. Okamura, C.C. Rowe, Assessing reactive astrogliosis with (18)F-SMBT-1 across the Alzheimer's disease spectrum, J. Nucl. Med. 63 (10) (2022) 1560–1569.

[26] P. Chatterjee, S. Pedrini, E. Stoops, K. Goozee, V.L. Villemagne, P.R. Asih, I.M. W. Verberk, P. Dave, K. Taddei, H.R. Sohrabi, H. Zetterberg, K. Blennow, C. E. Teunissen, H.M. Vanderstichele, R.N. Martins, Plasma glial fibrillary acidic protein is elevated in cognitively normal older adults at risk of Alzheimer's disease, Transl. Psychiatry 11 (1) (2021) 27.

[27] Y. Kong, C.A. Maschio, X. Shi, F. Xie, C. Zuo, U. Konietzko, K. Shi, A. Rominger, J. Xiao, Q. Huang, R.M. Nitsch, Y. Guan, R. Ni, Relationship between reactive astrocytes, by [(18)F]SMBT-1 imaging, with amyloid-beta, tau, glucose metabolism, and TSPO in mouse models of Alzheimer's disease, Mol. Neurobiol. (2024).

[28] K. Santacruz, J. Lewis, T. Spires, J. Paulson, L. Kotilinek, M. Ingelsson, A. Guimaraes, M. DeTure, M. Ramsden, E. McGowan, C. Forster, M. Yue, J. Orne, C. Janus, A. Mariash, M. Kuskowski, B. Hyman, M. Hutton, K.H. Ashe, Tau suppression in a neurodegenerative mouse model improves memory function, Science 309 (5733) (2005) 476–481.

[29] K. Tagai, M. Ono, M. Kubota, S. Kitamura, K. Takahata, C. Seki, Y. Takado, H. Shinotoh, Y. Sano, Y. Yamamoto, K. Matsuoka, H. Takuwa, M. Shimojo, M. Takahashi, K. Kawamura, T. Kikuchi, M. Okada, H. Akiyama, H. Suzuki, M. Onaya, T. Takeda, K. Arai, N. Arai, N. Araki, Y. Saito, J.Q. Trojanowski, V.M. Y. Lee, S.K. Mishra, Y. Yamaguchi, Y. Kimura, M. Ichise, Y. Tomita, M.R. Zhang, T. Suhara, M. Shigeta, N. Sahara, M. Higuchi, H. Shimada, High-contrast in vivo imaging of tau pathologies in Alzheimer's and non-Alzheimer's disease tauopathies, Neuron 109 (1) (2021) 42–58.e8.

[30] S. Rojas, J.R. Herance, J.D. Gispert, S. Abad, E. Torrent, X. Jiménez, D. Pareto, U. Perpiña, S. Sarroca, E. Rodríguez, A. Ortega-Aznar, C. Sanfeliu, In vivo evaluation of amyloid deposition and brain glucose metabolism of 5XFAD mice using positron emission tomography, Neurobiol. Aging 34 (7) (2013) 1790–1798.

[31] S. Jawhar, A. Trawicka, C. Jenneckens, T.A. Bayer, O. Wirths, Motor deficits, neuron loss, and reduced anxiety coinciding with axonal degeneration and intraneuronal Aβ aggregation in the 5XFAD mouse model of Alzheimer's disease, Neurobiol. Aging 33 (1) (2012), 196.e29–40.

[32] H. Oakley, S.L. Cole, S. Logan, E. Maus, P. Shao, J. Craft, A. Guillozet-Bongaarts, M. Ohno, J. Disterhoft, L. Van Eldik, R. Berry, R. Vassar, Intraneuronal beta-amyloid aggregates, neurodegeneration, and neuron loss in transgenic mice with five familial Alzheimer's disease mutations: potential factors in amyloid plaque formation, J. Neurosci. 26 (40) (2006) 10129–10140.

[33] K. Kawamura, H. Hashimoto, K. Furutsuka, T. Ohkubo, T. Fujishiro, T. Togashi, D. Arashi, T. Sakai, M. Muto, M. Ogawa, Y. Kurihara, N. Nengaki, M. Takei, K. Nemoto, M. Higuchi, M.R. Zhang, Radiosynthesis and quality control testing of the tau imaging positron emission tomography tracer [(18) F]PM-PBB3 for clinical applications, J Labelled Comp Radiopharm 64 (3) (2021) 109–119.

[34] Y. Liu, L. Zhu, K. Plössl, S.R. Choi, H. Qiao, X. Sun, S. Li, Z. Zha, H.F. Kung, Optimization of automated radiosynthesis of [18F]AV-45: a new PET imaging agent for Alzheimer's disease, Nucl. Med. Biol. 37 (8) (2010) 917–925.

[35] Y. Kong, L. Cao, F. Xie, X. Wang, C. Zuo, K. Shi, A. Rominger, Q. Huang, J. Xiao, D. Jiang, Y. Guan, R. Ni, Reduced SV2A and GABAA receptor levels in the brains of type 2 diabetic rats revealed by [18F]SDM-8 and [18F]flumazenil PET, Biomed. Pharmacother. 172 (2024) 116252.

[36] W. Hu, D. Pan, Y. Wang, W. Bao, C. Zuo, Y. Guan, F. Hua, M. Yang, J. Zhao, PET imaging for dynamically monitoring neuroinflammation in APP/PS1 mouse model using [(18)F]DPA714, Front. Neurosci. 14 (2020) 810.

[37] Y. Kong, L. Huang, W. Li, X. Liu, Y. Zhou, C. Liu, S. Zhang, F. Xie, Z. Zhang, D. Jiang, W. Zhou, R. Ni, C. Zhang, B. Sun, J. Wang, Y. Guan, The synaptic vesicle

[38] protein 2A interacts with key pathogenic factors in Alzheimer's disease: implications for treatment, Front. Cell Dev. Biol. 9 (2021) 609908.

[38] V. Kecheliev, L. Boss, U. Maheshwari, U. Konietzko, A. Keller, D. Razansky, R. M. Nitsch, J. Klohs, R. Ni, Aquaporin 4 is differentially increased and dislocated in association with tau and amyloid-beta, Life Sci. 121593 (2023).

[39] K. Tagai, M. Ono, M. Kubota, S. Kitamura, K. Takahata, C. Seki, Y. Takado, H. Shinotoh, Y. Sano, Y. Yamamoto, K. Matsuoka, H. Takuwa, M. Shimojo, M. Takahashi, K. Kawamura, T. Kikuchi, M. Okada, H. Akiyama, H. Suzuki, M. Onaya, T. Takeda, K. Arai, N. Arai, N. Araki, Y. Saito, J.Q. Trojanowski, V.M. Y. Lee, S.K. Mishra, Y. Yamaguchi, Y. Kimura, M. Ichise, Y. Tomita, M.R. Zhang, T. Suhara, M. Shigeta, N. Sahara, M. Higuchi, H. Shimada, High-contrast in vivo imaging of tau pathologies in Alzheimer's and non-Alzheimer's disease tauopathies, Neuron 109 (1) (2021) 42–58.e8.

[40] C.C. Weng, I.T. Hsiao, Q.F. Yang, C.H. Yao, C.Y. Tai, M.F. Wu, T.C. Yen, M.K. Jang, K.J. Lin, Characterization of (18)F-PM-PBB3 ((18)F-APN-1607) uptake in the rTg4510 mouse model of Tauopathy, Molecules 25 (7) (2020).

[41] A.L. Oblak, P.B. Lin, K.P. Kotredes, R.S. Pandey, D. Garceau, H.M. Williams, A. Uyar, R. O'Rourke, S. O'Rourke, C. Ingraham, D. Bednarczyk, M. Belanger, Z. A. Cope, G.J. Little, S.-P.G. Williams, C. Ash, A. Bleckert, T. Ragan, B.A. Logsdon, L. M. Mangravite, S.J. Sukoff Rizzo, P.R. Territo, G.W. Carter, G.R. Howell, M. Sasner, B.T. Lamb, Comprehensive evaluation of the 5XFAD mouse model for preclinical testing applications: a MODEL-AD study, Front. Aging Neurosci. 13 (2021) 431.

[42] K.P. Ng, T.A. Pascoal, S. Mathotaarachchi, J. Therriault, M.S. Kang, M. Shin, M. C. Guiot, Q. Guo, R. Harada, R.A. Comley, G. Massarweh, J.P. Soucy, N. Okamura, S. Gauthier, P. Rosa-Neto, Monoamine oxidase B inhibitor, selegiline, reduces 18F-THK5351 uptake in the human brain, Alzheimer's Res. Therapy 9 (1) (2017).

[43] S. Kasai, T. Yoshihara, O. Lopatina, K. Ishihara, H. Higashida, Selegiline ameliorates depression-like behavior in mice lacking the CD157/BST1 gene, a risk factor for Parkinson's disease, Front. Behav. Neurosci. 11 (2017) 75.

[44] I. Lamensdorf, S. Porat, R. Simantov, J.P. Finberg, Effect of low-dose treatment with selegiline on dopamine transporter (DAT) expression and amphetamine-induced dopamine release in vivo, Br. J. Pharmacol. 126 (4) (1999) 997–1002.

[45] S. Kang, J. Kim, S.Y. Lee, N. Okamura, K.A. Chang, MicroPET imaging assessment of brain tau and amyloid deposition in 6 × Tg Alzheimer's disease model mice, Int. J. Mol. Sci. 23 (10) (2022).

[46] F.R. López-Picón, T. Keller, D. Bocancea, J.S. Helin, A. Krzyczmonik, S. Helin, A. Damont, F. Dollé, J.O. Rinne, M. Haaparanta-Solin, O. Solin, Direct comparison of [(18)F]F-DPA with [(18)F]DPA-714 and [(11)C]PBR28 for neuroinflammation imaging in the same Alzheimer's disease model mice and healthy controls, Mol. Imaging Biol. 24 (1) (2022) 157–166.

[47] M. Brendel, F. Probst, A. Jaworska, F. Overhoff, V. Korzhova, N.L. Albert, R. Beck, S. Lindner, F.J. Gildehaus, K. Baumann, P. Bartenstein, G. Kleinberger, C. Haass, J. Herms, A. Rominger, Glial activation and glucose metabolism in a transgenic amyloid mouse model: a triple-tracer PET study, J. Nucl. Med. 57 (6) (2016) 954–960.

[48] T. Keller, F.R. López-Picón, A. Krzyczmonik, S. Forsback, A.K. Kirjavainen, J. S. Takkinen, O. Alzghool, J. Rajander, S. Teperi, F. Cacheux, A. Damont, F. Dollé, J. O. Rinne, O. Solin, M. Haaparanta-Solin, [18F]F-DPA for the detection of activated microglia in a mouse model of Alzheimer's disease, Nucl. Med. Biol. 67 (2018) 1–9.

[49] H. Endepols, M. Anglada-Huguet, E. Mandelkow, Y. Schmidt, P. Krapf, B. D. Zlatopolskiy, B. Neumaier, E.-M. Mandelkow, A. Drzezga, Assessment of the in vivo relationship between cerebral Hypometabolism, tau deposition, TSPO expression, and synaptic density in a tauopathy mouse model: a multi-tracer PET study, Mol. Neurobiol. 59 (6) (2022) 3402–3413.

[50] A. Ishikawa, M. Tokunaga, J. Maeda, T. Minamihisamatsu, M. Shimojo, H. Takuwa, M. Ono, R. Ni, S. Hirano, S. Kuwabara, B. Ji, M.R. Zhang, I. Aoki, T. Suhara, M. Higuchi, N. Sahara, In vivo visualization of tau accumulation, microglial activation, and brain atrophy in a mouse model of tauopathy rTg4510, J. Alzheimers Dis. 61 (3) (2018) 1037–1052.

[51] C. Bouter, C. Irwin, T.N. Franke, N. Beindorff, Y. Bouter, Quantitative brain positron emission tomography in female 5XFAD Alzheimer mice: pathological features and sex-specific alterations, Front Med (Lausanne) 8 (2021) 745064.

[52] G.R. Frost, V. Longo, T. Li, L.A. Jonas, M. Judenhofer, S. Cherry, J. Koutcher, C. Lekaye, P. Zanzonico, Y.-M. Li, Hybrid PET/MRI enables high-spatial resolution, quantitative imaging of amyloid plaques in an Alzheimer's disease mouse model, Sci. Rep. 10 (1) (2020) 10379.

[53] T.N. Franke, C. Irwin, T.A. Bayer, W. Brenner, N. Beindorff, C. Bouter, Y. Bouter, In vivo imaging with 18F-FDG- and 18F-Florbetaben-PET/MRI detects pathological changes in the brain of the commonly used 5XFAD mouse model of Alzheimer's disease, Front. Med. 7 (2020) 529.

[54] S.J. Oh, H.-J. Lee, K.J. Kang, S.J. Han, Y.J. Lee, K.C. Lee, S.M. Lim, D.Y. Chi, K. M. Kim, J.-A. Park, J.Y. Choi, Early detection of Aβ deposition in the 5xFAD mouse by amyloid PET, Contrast Media Mol. Imag. 2018 (2018) 5272014.

[55] R. Ni, B. Ji, M. Ono, N. Sahara, M.R. Zhang, I. Aoki, A. Nordberg, T. Suhara, M. Higuchi, Comparative in vitro and in vivo quantifications of pathologic tau deposits and their association with neurodegeneration in tauopathy mouse models, J. Nucl. Med. 59 (6) (2018) 960–966.

[56] T. Kimura, M. Ono, C. Seki, K. Sampei, M. Shimojo, K. Kawamura, M.R. Zhang, N. Sahara, Y. Takado, M. Higuchi, A quantitative in vivo imaging platform for tracking pathological tau depositions and resultant neuronal death in a mouse model, Eur. J. Nucl. Med. Mol. Imaging 49 (13) (2022) 4298–4311.

[57] R.J. Tyacke, J.F.M. Myers, A. Venkataraman, I. Mick, S. Turton, J. Passchier, S. M. Husbands, E.A. Rabiner, R.N. Gunn, P.S. Murphy, C.A. Parker, D.J. Nutt, Evaluation of (11)C-BU99008, a PET ligand for the imidazoline(2) binding site in human brain, J. Nucl. Med. 59 (10) (2018) 1597–1602.

[58] L. Park, K. Hochrainer, Y. Hattori, S.J. Ahn, A. Anfray, G. Wang, K. Uekawa, J. Seo, V. Palfini, I. Blanco, D. Acosta, D. Eliezer, P. Zhou, J. Anrather, C. Iadecola, Tau induces PSD95-neuronal NOS uncoupling and neurovascular dysfunction independent of neurodegeneration, Nat. Neurosci. 23 (9) (2020) 1079–1089.

[59] L.J. Blair, H.D. Frauen, B. Zhang, B.A. Nordhues, S. Bijan, Y.C. Lin, F. Zamudio, L. D. Hernandez, J.J. Sabbagh, M.L. Selenica, C.A. Dickey, Tau depletion prevents progressive blood-brain barrier damage in a mouse model of tauopathy, Acta Neuropathol. Commun. 3 (2015) 8.

[60] S. Forner, S. Kawauchi, G. Balderrama-Gutierrez, E.A. Kramár, D.P. Matheos, J. Phan, D.I. Javonillo, K.M. Tran, E. Hingco, C. da Cunha, N. Rezaie, J. A. Alcantara, D. Baglietto-Vargas, C. Jansen, J. Neumann, M.A. Wood, G. R. MacGregor, A. Mortazavi, A.J. Tenner, F.M. LaFerla, K.N. Green, Systematic phenotyping and characterization of the 5xFAD mouse model of Alzheimer's disease, Sci Data 8 (1) (2021) 270.

[61] A. Chaney, M. Bauer, D. Bochicchio, A. Smigova, M. Kassiou, K.E. Davies, S. R. Williams, H. Boutin, Longitudinal investigation of neuroinflammation and metabolite profiles in the APP(swe) ×PS1(Δe9) transgenic mouse model of Alzheimer's disease, J. Neurochem. 144 (3) (2018) 318–335.

[62] A.M. Chaney, F.R. Lopez-Picon, S. Serrière, R. Wang, D. Bochicchio, S.D. Webb, M. Vandesquille, M.K. Harte, C. Georgiadou, C. Lawrence, J. Busson, J. Vercouillie, C. Tauber, F. Buron, S. Routier, T. Reekie, A. Snellman, M. Kassiou, J. Rokka, K. E. Davies, J.O. Rinne, D.A. Salih, F.A. Edwards, L.D. Orton, S.R. Williams, S. Chalon, H. Boutin, Prodromal neuroinflammatory, cholinergic and metabolite dysfunction detected by PET and MRS in the TgF344-AD transgenic rat model of AD: a collaborative multi-modal study, Theranostics 11 (14) (2021) 6644–6667.

[63] Y. Yoshiyama, M. Higuchi, B. Zhang, S.M. Huang, N. Iwata, T.C. Saido, J. Maeda, T. Suhara, J.Q. Trojanowski, V.M. Lee, Synapse loss and microglial activation precede tangles in a P301S tauopathy mouse model, Neuron 53 (3) (2007) 337–351.

[64] J. Benetatos, R.E. Bennett, H.T. Evans, S.A. Ellis, B.T. Hyman, L.G. Bodea, J. Götz, PTEN activation contributes to neuronal and synaptic engulfment by microglia in tauopathy, Acta Neuropathol. 140 (1) (2020) 7–24.

[65] L. Rejc, V. Gómez-Vallejo, A. Joya, G. Arsequell, A. Egimendia, P. Castellnou, X. Ríos-Anglada, U. Cossío, Z. Baz, L. Iglesias, E. Capetillo-Zarate, P. Ramos-Cabrer, A. Martin, J. Llop, Longitudinal evaluation of neuroinflammation and oxidative stress in a mouse model of Alzheimer disease using positron emission tomography, Alzheimers Res. Ther. 14 (1) (2022) 80.

[66] N. Mirzaei, S.P. Tang, S. Ashworth, C. Coello, C. Plisson, J. Passchier, V. Selvaraj, R.J. Tyacke, D.J. Nutt, M. Sastre, In vivo imaging of microglial activation by positron emission tomography with [(11)C]PBR28 in the 5XFAD model of Alzheimer's disease, Glia 64 (6) (2016) 993–1006.

[67] L.H. Fairley, N. Sahara, I. Aoki, B. Ji, T. Suhara, M. Higuchi, A.M. Barron, Neuroprotective effect of mitochondrial translocator protein ligand in a mouse model of tauopathy, J. Neuroinflammation 18 (1) (2021) 76.

[68] B.B. Tournier, S. Tsartsalis, K. Ceyzériat, B.H. Fraser, M.C. Grégoire, E. Kövari, P. Millet, Astrocytic TSPO upregulation appears before microglial TSPO in Alzheimer's disease, J. Alzheimers Dis. 77 (3) (2020) 1043–1056.

[69] M. Pannell, V. Economopoulos, T.C. Wilson, V. Kersemans, P.G. Isenegger, J. R. Larkin, S. Smart, S. Gilchrist, V. Gouverneur, N.R. Sibson, Imaging of translocator protein upregulation is selective for pro-inflammatory polarized astrocytes and microglia, Glia 68 (2) (2020) 280–297.

[70] G. Biechele, N. Franzmeier, T. Blume, M. Ewers, J.M. Luque, F. Eckenweber, C. Sacher, L. Beyer, F. Ruch-Rubinstein, S. Lindner, F.J. Gildehaus, B. von Ungern-Sternberg, P. Cumming, P. Bartenstein, A. Rominger, G.U. Höglinger, J. Herms, M. Brendel, Glial activation is moderated by sex in response to amyloidosis but not to tau pathology in mouse models of neurodegenerative diseases, J. Neuroinflammation 17 (1) (2020) 374.

[71] H. Endepols, M. Anglada-Huguet, E. Mandelkow, B. Neumaier, E.M. Mandelkow, A. Drzezga, Fragmentation of functional resting state brain networks in a transgenic mouse model of tau pathology: a metabolic connectivity study using [(18)F]FDG-PET, Exp. Neurol. 372 (2024) 114632.

[72] M. Shimojo, H. Takuwa, Y. Takado, M. Tokunaga, S. Tsukamoto, K. Minatohara, M. Ono, C. Seki, J. Maeda, T. Urushihata, T. Minamihisamatsu, I. Aoki, K. Kawamura, M.R. Zhang, T. Suhara, N. Sahara, M. Higuchi, Selective disruption of inhibitory synapses leading to neuronal hyperexcitability at an early stage of tau pathogenesis in a mouse model, J. Neurosci. 40 (17) (2020) 3491–3501.

[73] D. Kindler, C. Maschio, R. Ni, V. Zerbi, D. Razansky, J. Klohs, Arterial spin labeling demonstrates preserved regional cerebral blood flow in the P301L mouse model of tauopathy, J. Cereb. Blood Flow Metab. 42 (4) (2021) 686–693.

[74] A. Jullienne, J.I. Szu, R. Quan, M.V. Trinh, T. Norouzi, B.P. Noarbe, A.A. Bedwell, K. Eldridge, S.C. Persohn, P.R. Territo, A. Obenaus, Cortical cerebrovascular and metabolic perturbations in the 5xFAD mouse model of Alzheimer's disease, Front. Aging Neurosci. 15 (2023) 1220036.

[75] E.J. Chumin, C.P. Burton, R. Silvola, E.W. Miner, S.C. Persohn, M. Veronese, P. R. Territo, Brain metabolic network covariance and aging in a mouse model of Alzheimer's disease, Alzheimers Dement 20 (3) (2024) 1538–1549.

[76] T.N. Franke, C. Irwin, T.A. Bayer, W. Brenner, N. Beindorff, C. Bouter, Y. Bouter, In vivo imaging with (18)F-FDG- and (18)F-Florbetaben-PET/MRI detects pathological changes in the brain of the commonly used 5XFAD mouse model of Alzheimer's disease, Front Med (Lausanne) 7 (2020) 529.

[77] I.R. Macdonald, D.R. DeBay, G.A. Reid, T.P. O'Leary, C.T. Jollymore, G. Mawko, S. Burrell, E. Martin, C.V. Bowen, R.E. Brown, S. Darvesh, Early detection of cerebral glucose uptake changes in the 5XFAD mouse, Curr. Alzheimer Res. 11 (5) (2014) 450–460.

[78] H. Choi, Y. Choi, E.J. Lee, H. Kim, Y. Lee, S. Kwon, D.W. Hwang, D.S. Lee, Hippocampal glucose uptake as a surrogate of metabolic change of microglia in Alzheimer's disease, J. Neuroinflammation 18 (1) (2021) 190.

[79] J. Gnörich, A. Reifschneider, K. Wind, A. Zatcepin, S.T. Kunte, P. Beumers, L. M. Bartos, T. Wiedemann, M. Grosch, X. Xiang, M.K. Fard, F. Ruch, G. Werner, M. Koehler, L. Slemann, S. Hummel, N. Briel, T. Blume, Y. Shi, G. Biechele, L. Beyer, F. Eckenweber, M. Scheifele, P. Bartenstein, N.L. Albert, J. Herms, S. Tahirovic, C. Haass, A. Capell, S. Ziegler, M. Brendel, Depletion and activation of microglia impact metabolic connectivity of the mouse brain, J. Neuroinflammation 20 (1) (2023) 47.

[80] S. Sérrière, C. Tauber, J. Vercouillie, C. Mothes, C. Pruckner, D. Guilloteau, M. Kassiou, A. Doméné, L. Garreau, G. Page, S. Chalon, Amyloid load and translocator protein 18 kDa in APPswePS1-dE9 mice: a longitudinal study, Neurobiol. Aging 36 (4) (2015) 1639–1652.

[81] F.R. López-Picón, A. Snellman, O. Eskola, A. Helin, O. Solin, M. Haaparanta-Solin, J.O. Rinne, Neuroinflammation appears early on PET imaging and then plateaus in a mouse model of Alzheimer disease, J. Nucl. Med. 59 (3) (2018) 509.

[82] I.J. Hildebrandt, H. Su, W.A. Weber, Anesthesia and other considerations for in vivo imaging of small animals, ILAR J. 49 (1) (2008) 17–26.

[83] K. Varnäs, S.J. Finnema, P. Johnström, R. Arakawa, C. Halldin, L.I. Eriksson, L. Farde, Effects of sevoflurane anaesthesia on radioligand binding to monoamine oxidase-B in vivo, Br. J. Anaesth. 126 (1) (2021) 238–244.